Combined effects of tectonics and glacial isostatic adjustment on intraplate deformation in central and northern Europe: Applications to geodetic baseline analyses

A. M. Marotta,[1] J. X. Mitrovica,[2] R. Sabadini,[1] and G. Milne[3]

Received 6 December 2002; revised 1 July 2003; accepted 17 October 2003; published XX Month 2004.

[1] We use a suite of spherical, thin sheet, finite element model calculations to investigate the pattern of horizontal tectonic deformation within Europe. The calculations incorporate the effects of Africa-Eurasia convergence, Atlantic Ridge push forces, and changes in the lithospheric strength of the East European and Mediterranean subdomains. These predictions are compared to the deformation computed for the same region using a spherically symmetric, self-gravitating, viscoelastic Earth model of glacial isostatic adjustment. The radial viscosity profile and ice history input into the GIA model are taken from a model that "best fits" three-dimensional crustal velocities estimated from the BIFROST Fennoscandian GPS network. The comparison of the tectonic and GIA signals includes predictions of both crustal velocity maps and baseline length changes associated with sites within the permanent ITRF2000 and BIFROST GPS networks. Our baseline analysis includes reference sites in northern and central Europe that are representative of sites at the center, edge, and periphery of the GIA-induced deformation. Baseline length change predictions associated with all three reference sites are significantly impacted by both tectonic and GIA effects, albeit with distinct geometric sensitivities. In this regard, several of our tectonic models yield baseline rates from Vaas, Onsala, and Potsdam to sites below 55°N which are consistent with observed trends. We find that a best fit to the ITRF2000 data set is obtained by simultaneously considering the effects of GIA plus tectonics, where the latter is modeled with a relatively weak Mediterranean subdomain. In this case, the tectonic model contributes to the observed shortening between Onsala/Potsdam and sites to the south, without corrupting the extension observed for baselines extending from these reference sites and sites to the north; this extension is well reconciled by the GIA process alone. *INDEX TERMS:* 1208 Geodesy and Gravity: Crustal movements—intraplate (8110); 3210 Mathematical Geophysics: Modeling; 8110 Tectonophysics: Continental tectonics—general (0905); 9335 Information Related to Geographic Region: Europe; *KEYWORDS:* tectonics, GIA, intraplate deformation

Citation: Marotta, A. M., J. X. Mitrovica, R. Sabadini, and G. Milne (2004), Combined effects of tectonics and glacial isostatic adjustment on intraplate deformation in central and northern Europe: Applications to geodetic baseline analyses, *J. Geophys. Res.*, *109*, XXXXXX, doi:10.1029/2002JB002337.

1. Introduction

[2] Crustal deformation patterns in Europe are influenced by both plate tectonic forces and glacial isostatic adjustment, with the former including boundary forces associated with Africa-Eurasia convergence and spreading at the Mid-Atlantic Ridge. The region has been monitored by surveying using permanent global positioning system (GPS) receivers of the ITRF2000 network, established by the International Earth Rotation Service (IERSE *Altamimi et al.*, 2002]). Furthermore, we make use of the available BIFROST data, which provide additional stations not included in the ITRF network [*Johansson et al.*, 2002; *Milne et al.*, 2001].

[3] In principle, baseline length changes (henceforth baseline rates) for pairs of sites within these networks can be compared to predictions obtained from tectonic models (driven by Africa-Eurasia convergence, Atlantic Ridge opening, etc.) and GIA simulations in order to investigate the nature and origin of intraplate deformation in continental Europe. In the past, this effort has treated either tectonic and GIA effects in isolation. For example, *Milne et al.* [2001] analyzed three-dimensional (3-D) crustal deformation estimated from the BIFROST network using a suite of GIA models; they concluded, on the basis of residual maps

[1]Geophysics Section, Department of Earth Sciences, University of Milan, Milan, Italy.
[2]Department of Physics, University of Toronto, Toronto, Ontario, Canada.
[3]Department of Geological Sciences, University of Durham, Durham, UK.

0148-0227/04/2002JB002337$09.00

constructed by subtracting their best fit GIA model from the observations, that horizontal neotectonic motions were less than 1 mm/yr. In any case, predictions of 3-D motions associated with GIA in Europe have commonly treated geodetic baselines that extend well into central Europe [e.g., *James and Lambert*, 1993; *Mitrovica et al.*, 1994b; *Peltier*, 1995].

[4] Clearly, these analyses raise several important questions. Is there a region in northern Europe where tectonic effects on baseline rates can be ignored, or in southern Europe where the GIA signal is unimportant? Is there a transition region where both are important? More generally, what is the complex geometric interplay between tectonics and GIA in European continental deformation? In this paper we investigate these issues by extending earlier work [*Marotta and Sabadini*, 2002] to compare predictions generated from a large sequence of thin sheet models [*England and McKenzie*, 1983; *Marotta et al.*, 2001] to a GIA simulation based on a recent analysis of the BIFROST data set [*Milne et al.*, 2001]. The thin sheet models include Africa-Eurasia convergence and they explore the sensitivity of the predictions to both changes in the velocity forcing along the Atlantic Ridge and variations in the lithospheric strength of various European subdomains. Our analysis highlights a combined GIA plus tectonics model which best fits (within our search of model space) the ITRF2000 data.

2. Model Setup

2.1. Finite Element Tectonic Model

[5] We adopt an incompressible, viscous model to investigate tectonic deformation in the Mediterranean and Fennoscandian region driven by Africa-Eurasia convergence and Mid-Atlantic Ridge opening (Figure 1). (The treatment of the lithosphere as an incompressible, viscous fluid is widely adopted in models of long timescale geological processes [*Turcotte and Schubert*, 2002].) The deformation field is expressed in terms of crustal velocities and baseline rates obtained from a thin sheet approximation implemented by *Marotta et al.* [2001] and modified here to consider a spherical geometry. This implementation treats the lithosphere as a stratified viscous sheet with constant total thickness, overlying an inviscid asthenosphere; the latter assures a stress-free condition at the base of the plate. Our thin sheet approximation assumes that the lithospheric thickness is small compared to the lateral wavelength of the applied loads, and thus vertical gradients of horizontal velocity and deviatoric viscous stresses are neglected. Isostatic compensation of the crust is also assumed.

[6] The western and southern borders of the model domain are chosen to coincide with the location of the Mid-Atlantic Ridge and the Africa-Eurasia plate contact respectively. Velocity boundary conditions are applied along these boundaries. The right border of the model domain lies along the 45°E meridian, inside the intracratonic East European Platform, where the transmission of stress from the applied boundary forcing is expected to be relatively small. The domain is discretized using planar finite triangular elements sufficiently small in size (no bigger than $1^\circ \times 1^\circ$ in central and northern Europe and $2^\circ \times 2^\circ$ in the western oceanic portion of the domain) to justify treating the surface of each individual grid element as flat.

[7] Next, we turn to a review of the governing equations used in this study. In spherical coordinates the deviatoric components of stress are related to the velocity components u_r, u_θ, and u_ϕ by

$$\tau_{\theta\theta} = \frac{2\mu}{r}\left(\frac{\partial}{\partial\theta}u_\theta + u_r\right) \tag{1}$$

$$\tau_{\phi\phi} = \frac{2\mu}{r}\left(\frac{1}{\sin\theta}\frac{\partial}{\partial\phi}u_\phi + u_\theta\cot\theta + u_r\right) \tag{2}$$

$$\tau_{rr} = 2\mu\frac{\partial}{\partial r}u_r \tag{3}$$

$$\tau_{\theta\phi} = \frac{\mu}{r}\left(\frac{1}{\sin\theta}\frac{\partial}{\partial\phi}u_\theta + \frac{\partial}{\partial\theta}u_\phi - u_\phi\cot\theta\right) \tag{4}$$

$$\tau_{\theta r} = \frac{\mu}{r}\left(r\frac{\partial}{\partial r}u_\theta + \frac{\partial}{\partial\theta}u_r - u_\theta\right) \tag{5}$$

$$\tau_{\phi r} = \frac{\mu}{r}\left(r\frac{\partial}{\partial r}u_\phi + \frac{1}{\sin\theta}\frac{\partial}{\partial\phi}u_r - u_\phi\right) \tag{6}$$

where μ denotes the viscosity and θ, ϕ, and r represent the colatitude (south), east longitude, and radial distance from the Earth's center. In the same coordinate system the θ, ϕ, and r components of the momentum equations are then [*Schubert et al.*, 2001]

$$\frac{1}{r}\frac{\partial}{\partial\theta}\sigma_{\theta\theta} + \frac{1}{r\sin\theta}\frac{\partial}{\partial\phi}\sigma_{\theta\phi} + \frac{\partial}{\partial r}\sigma_{\theta r} + \frac{1}{r}\left[(\sigma_{\theta\theta} - \sigma_{\phi\phi})\cot\theta + 3\sigma_{\theta r}\right] = 0 \tag{7}$$

$$\frac{1}{r}\frac{\partial}{\partial\theta}\sigma_{\phi\theta} + \frac{1}{r\sin\theta}\frac{\partial}{\partial\phi}\sigma_{\phi\phi} + \frac{\partial}{\partial r}\sigma_{\phi r} + \frac{1}{r}(3\sigma_{\phi r} + 2\sigma_{\phi\theta}\cot\theta) = 0 \tag{8}$$

$$\frac{1}{r}\frac{\partial}{\partial\theta}\sigma_{r\theta} + \frac{1}{r\sin\theta}\frac{\partial}{\partial\phi}\sigma_{r\phi} + \frac{\partial}{\partial r}\sigma_{rr} + \frac{1}{r}(2\sigma_{rr} - \sigma_{\theta\theta} - \sigma_{\phi\phi} + \sigma_{r\theta}\cot\theta) + f_r = 0 \tag{9}$$

where f_r denotes the gravitational body force term. As usual, the stress can be written as

$$\sigma_{ij} = \tau_{ij} - p_0\delta_{ij} \tag{10}$$

where p_0 is the hydrostatic pressure.

[8] Under our assumption that only horizontal tectonic forces are active, and since basal shear stresses are absent, the components $\sigma_{r\theta}$ and $\sigma_{r\phi}$ within these general equations may be neglected. As detailed in Appendix A, applying both the constitutive equation for an incompressible, viscous material and the conditions for isostatic balance, the

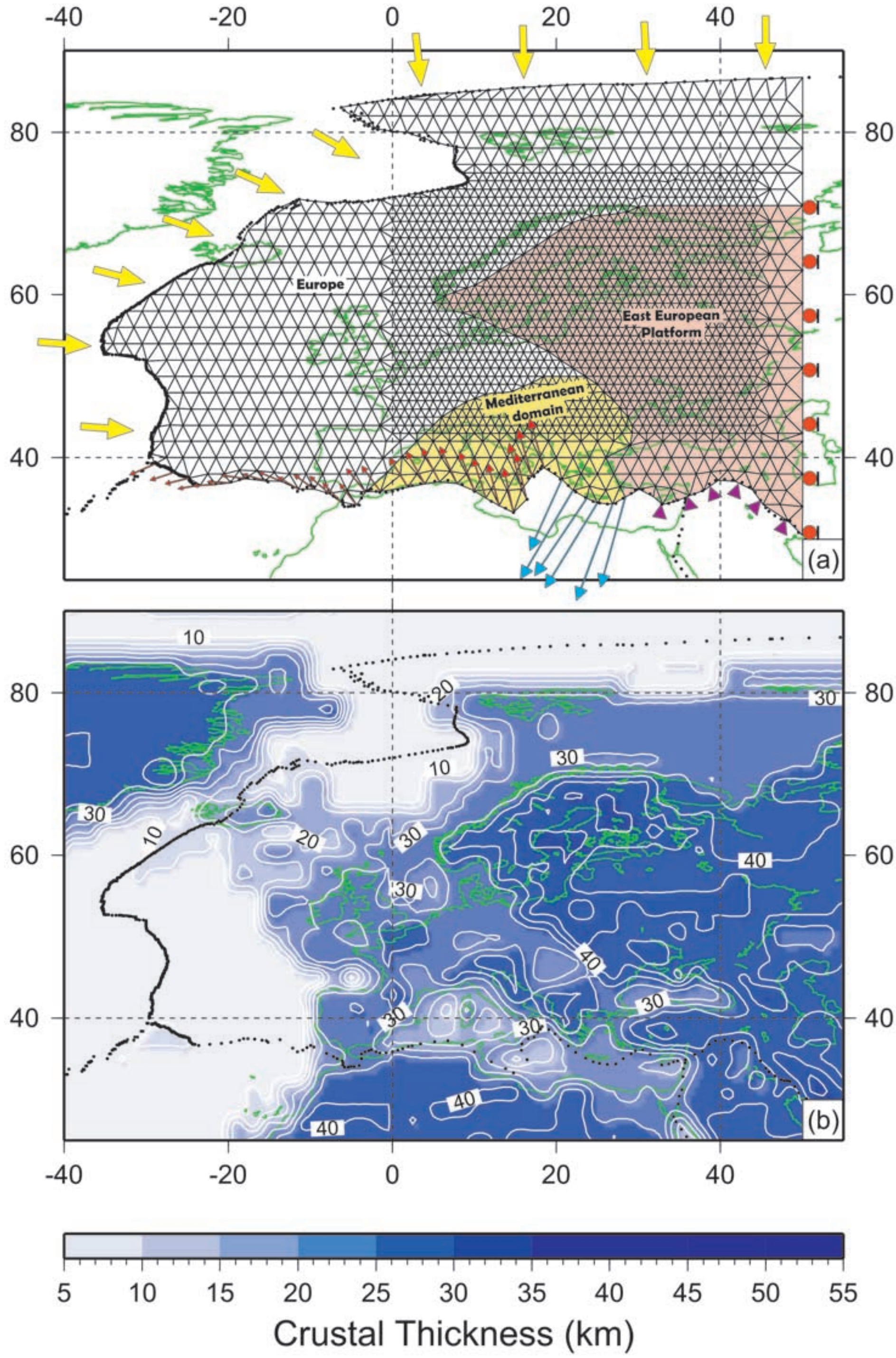

Figure 1. (a) Finite element grid adopted for the tectonic predictions described in this study. The grid distinguishes three major blocks, or subdomains: The European, East European Platform, and Mediterranean. The yellow arrows at the left side of the domain represent ridge push forces. The counterclockwise rotation of the African plate with respect to the European plate, adopted from NUVEL-1A, is reflected by the red arrows at bottom left. The velocities along the Aegean Trench (blue arrows) were geodetically determined by *McClusky et al.* [2000]. The southern border between the model domain and the Arabian region is held fixed (pink triangles), while the right (eastern) boundary of the model is assumed to be shear stress free (red dots). (b) Crustal thickness variation used in the analysis.

momentum equations reduce, after integration over the thickness of the lithosphere, to

$$\frac{\partial}{\partial\theta}\left[2\bar{\mu}\left(\frac{\partial}{\partial\theta}u_\theta+u_r\right)\right]+\frac{1}{\sin\theta}\frac{\partial}{\partial\phi}\left[\bar{\mu}\left(\frac{1}{\sin\theta}\frac{\partial}{\partial\phi}u_\theta+\frac{\partial}{\partial\theta}u_\phi - u_\phi\cot\theta\right)\right]+\left[2\bar{\mu}\left(\frac{\partial}{\partial\theta}u_\theta-\frac{1}{\sin\theta}\frac{\partial}{\partial\phi}u_\phi - u_\theta\cot\theta\right)\right]\cot\theta=\frac{g\rho_c R}{2L}\left(1-\frac{\rho_c}{\rho_m}\right)\frac{\partial}{\partial\theta}S^2 \tag{11}$$

$$\frac{\partial}{\partial\theta}\left[\bar{\mu}\left(\frac{1}{\sin\theta}\frac{\partial}{\partial\phi}u_\theta+\frac{\partial}{\partial\theta}u_\phi-u_\phi\cot\theta\right)\right]+\frac{1}{\sin\theta}\frac{\partial}{\partial\phi}\left[2\bar{\mu}\left(\frac{1}{\sin\theta}\frac{\partial}{\partial\phi}u_\phi + u_\theta\cot\theta+u_r\right)\right]+\left[2\bar{\mu}\left(\frac{\partial}{\partial\theta}u_\phi+\frac{1}{\sin\theta}\frac{\partial}{\partial\phi}u_\theta-u_\phi\cot\theta\right)\right]\cot\theta = \frac{g\rho_c R}{2L}\left(1-\frac{\rho_c}{\rho_m}\right)\frac{1}{\sin\theta}\frac{\partial}{\partial\phi}S^2 \tag{12}$$

where $\bar{\mu}$ denotes the vertically averaged viscosity of the lithosphere. In equations (11) and (12), S is the crustal thickness, L is the lithospheric thickness, ρ_c and ρ_m denote the densities of the crust and lithosphere, respectively, g is the gravity, and R is the radius of the Earth. The third unknown, u_r, is eliminated from these equations by invoking incompressibility and by assuming that the radial strain rate $(\partial/\partial r)u_r$ vanishes. Under these assumptions, u_r may be expressed as

$$u_r=-\frac{1}{2}\left\{\frac{\partial u_\theta}{\partial\theta}+\frac{1}{\sin\theta}\frac{\partial u_\phi}{\partial\phi}+u_\theta\cot\theta\right\} \tag{13}$$

Thus the thin sheet model is a reliable predictor of the horizontal components of velocity field u_θ, u_ϕ only.

[9] Once the crustal thickness S and boundary conditions are specified, the numerical integration of equations (11) and (12) yields the stationary tectonic deformation field. Within each finite element, the velocity is approximated by linear polynomial interpolating functions and numerical integration is performed by Gaussian quadrature with 7 integration points.

[10] We performed a series of 9 numerical "tectonic deformation" experiments summarized as models 1–7 and 16–17 in Table 1. The models are distinguished in terms of the adopted lithospheric viscosity and imposed velocity boundary condition along the North Atlantic Ridge. We next discuss each of these model inputs.

[11] A distinct viscosity can be applied to each element of the model grid, and this permits incorporation of lateral variations in lithospheric strength. For this purpose, the European lithosphere is treated as the reference subdomain with a prescribed reference (i.e., fixed) viscosity. We verified that for the homogeneous model the predicted velocity pattern is controlled by the velocity boundary conditions and that it is unaffected by changes in the lithospheric viscosity in the range 10^{23} to 10^{25} Pa s; we have chosen the value of 10^{25} Pa s as reference viscosity since it guarantees numerical stability once lateral viscosity variations are introduced.

[12] Two other (assumed isoviscous) lithospheric subdomains are considered in this analysis. The first corresponds

Table 1. List of Model Types Considered in the Analysis t1.1

Model	Rheological Heterogeneities	Ridge Velocity Boundary Conditions, mm/yr	
			t1.2
1	no rheological heterogeneities	0.0	t1.3
2	no rheological heterogeneities	1.0	t1.4
3	no rheological heterogeneities	5.0	t1.5
4	stiff East European Platform	0.0	t1.6
5	stiff East European Platform	5.0	t1.7
6	soft Mediterranean subdomain	0.0	t1.8
7	soft Mediterranean subdomain	5.0	t1.9
8	GIA, *Milne et al.* [2001]		t1.10
9	model 8 plus model 1		t1.11
10	model 8 plus model 2		t1.12
11	model 8 plus model 3		t1.13
12	model 8 plus model 4		t1.14
13	model 8 plus model 5		t1.15
14	model 8 plus model 6		t1.16
15	model 8 plus model 7		t1.17
16	model 4 plus model 6		t1.18
17	model 5 plus model 7		t1.19
18	model 8 plus model 16		t1.20
19	model 8 plus model 17		t1.21

to the so-called "Mediterranean subdomain," extending from the Tyrrhenian Sea to the eastern limit of the Pannonian Basin through the Adriatic Plate (Figure 1a). The Mediterranean subdomain is, in particular, an assemblage of different structural units (e.g., the Adriatic plate, Tyrrhenian Sea, and Pannonian Basin); however, our simplification is motivated by our focus on the long wavelength deformation pattern of the tectonic boundary forcing. The second lithospheric subdomain is the East European Platform, which encompasses most of the Caledonian Deformation Front (Figure 1a).

[13] We note that our modeling has some similarities to earlier work by *Grunthal and Stromeyer* [1992]. They modeled the stress field in central Europe by making use of an elastic rheology with laterally varying rigidities that simulated different tectonic units; in our analysis we adopt a viscous fluid with laterally varying strength and compare our predictions to geodetic observations.

[14] The velocity boundary conditions we apply are relative to the Eurasian plate, which is considered fixed. The velocity of Africa relative to Eurasia is prescribed by NUVEL-1A (red arrows, Figure 1a) and the pattern reflects an Africa-Eurasia continental convergence of the order 1 cm/yr. Note that these velocities impose a counterclockwise rotation of the Africa plate with respect to Eurasia. Relative to a fixed Eurasia, we also consider the ridge push forces acting along the North Atlantic Ridge. In our simulations these forces are parameterized in terms of velocity boundary conditions applied along the ridge; they thus simulate the line forces acting along the plate boundary, as described by *Richardson et al.* [1979]. (To emphasize that these velocity boundary conditions are not derived in the same manner as those related to Africa-Eurasia convergence, we make use of a different symbol along the Atlantic Ridge; specifically, the thick yellow arrows denote the parameterization of the line force in terms of velocities with respect to a fixed Eurasia.)

[15] The line forces normal to the ridge have been evaluated from the eigenvalues of the stress tensor within those elements whose left sides define the ridge. Along the westernmost part of the Atlantic Ridge, our predicted ridge push forces range from $\sim 10^{12}$ N/m, for an imposed velocity

boundary condition of about 1 mm/yr, to $\sim 10^{13}$ N/m or a velocity boundary condition of 5 mm/yr; this last value represents an upper bound for ridge push forces [*Richardson and Reding*, 1991]. We note that these imposed velocities are not taken as constant along the ridge but rather are scaled with respect to the spreading velocities deduced from NUVEL-1A. In this regard, imposed velocities of 1 and 5 mm/yr are of the order of 1/20th and 1/4th of the full spreading rate ($\sim$2 mm/yr) according to NUVEL-1A.

[16] Along the Aegean trench, velocities at six sites determined geodetically by *McClusky et al.* [2000] are applied to an equal number of nodes in their vicinity (blue arrows, Figure 1a), from west to east: LOGO (25 mm/yr), LEON (33 mm/yr), OMAL (30 mm/yr), ROML (32 mm/yr), KAPT (33 mm/yr), and KATV (30 mm/yr). These velocities reflect trench subduction forces along this boundary and represent the velocity of these geodetic sites with respect to Eurasia.

[17] The eastern boundary of the model domain is held fixed. To avoid large effects from artificial stress accumulation, we have imposed a shear stress free boundary condition at this location (as indicated by the red dots along the right boundary of the model). The imposed conditions along the eastern boundary would be consistent with a possible decoupling between the western and eastern parts of the Eurasia plate [*Molnar et al.*, 1973]; these conditions imply that we are assuming that all the intraplate deformation of Eurasia due to Africa-Eurasia convergence and Atlantic Ridge push takes place within the model domain.

[18] The contact between the East European Platform and Arabian Plate is held fixed, as indicated by the pink triangles in the southeast part of Figure 1a. NUVEL-1A indicates a north directed velocity on this boundary. However, as discussed by *Jiménez-Munt et al.* [2003], the local stiffness of the lithosphere and the existence of a transcurrent fault at the northern boundary of the Arabian Plate produce little long-wavelength deformation to the north, where the (ITRF2000 and BIFROST) sites we will be considering are located.

[19] Since we are considering Eurasia as fixed, our modeled velocity fields will not contain any rigid rotation of Eurasia with respect to a global reference frame. Rather, these motions will represent velocities (that is, intraplate deformations) superimposed on any rigid plate motions.

[20] Finally, the crustal thickness variation used in the analysis has been obtained by linear interpolation onto the adopted grid of model CRUST 2.0 [*Bassin et al.*, 2000; http://mahi.ucsd.edu/Gabi/rem.html] (Figure 1b).

2.2. Glacial Isostatic Adjustment

[21] We model glacial isostatic adjustment (GIA) using a Love number formalism [*Peltier*, 1974] valid for a spherically symmetric, self-gravitating and (Maxwell) viscoelastic Earth model. The model is elastically compressible, and the radial elastic structure is prescribed by the seismic model PREM [*Dziewonski and Anderson*, 1981]. We adopt a combination of Late Pleistocene ice history and radial viscosity profile that has been shown to provide an excellent fit to the three-dimensional crustal velocities estimated using the BIFROST Fennoscandian GPS network [*Johansson et al.*, 2002; *Milne et al.*, 2001]. Specifically, the ice model is composed of the global ICE-3G deglaciation model [*Tushingham and Peltier*, 1991] with the Fennoscandian history replaced by the model of *Lambeck et al.* [1998]. The viscosity profile is characterized by a high viscosity (effectively elastic) lithosphere of thickness 120 km, an upper mantle viscosity of 8×10^{20} Pa s, and a lower mantle viscosity of 10^{22} Pa s.

[22] The prediction of the three-dimensional crustal velocity field is based on a spectral formalism described by *Mitrovica et al.* [1994a] and extended to include rotational effects by *Mitrovica et al.* [2001]. This theory requires a gravitationally self-consistent ocean load component of the total (ice plus water) surface mass load and this is generated using the sea level theory described, in detail, by *Milne et al.* [1999].

3. Sample Model Results: Tectonic Crustal Velocity

[23] For the purposes of brevity, we will show velocity and baseline rate patterns for only a subset of the tectonic models listed in Table 1; our goal is to explore the impact of lateral viscosity variations and the boundary condition along the Atlantic Ridge on the predictions. In the final results section (section 6) we perform a statistical analysis of predictions based on all the models in Table 1 in order to find the best fitting (relative to the geodetic constraints) combination of GIA and tectonics deformation models.

[24] The first three models in Table 1 are distinguished on the basis of the imposed velocity boundary condition along the North Atlantic Ridge. All other boundary conditions are as specified above. The horizontal velocities predicted for these three models are shown in Figures 2a–2c, respectively.

[25] Figure 2a isolates the influence of Africa-Eurasia convergence on the intraplate velocity pattern within the model domain. In this case, the predicted intensity of the crustal velocity gradually diminishes from $\sim$2 mm/yr at latitudes of 45° along the Alpine front to 0.2 mm/yr in central Fennoscandia. Clearly, the velocity field driven by the African indenter extends, with a northwestern direction, through the whole of central Europe, with the isocontours of velocity being roughly parallel to the collision front.

[26] When a velocity boundary condition of 1 mm/yr is applied along the North Atlantic Ridge (Figure 2b), in order to parameterize ridge push forces, we notice in central and northern Europe a rotation from NW to NE in the velocity pattern. Furthermore, with respect to Figure 2a, the velocity is increased throughout the western part of the study

Figure 2. Predictions of horizontal crustal velocities generated using our finite element tectonic model (arrows and color contouring). The models are all based on a homogeneous lithosphere with viscosity of 10^{25} Pa s, and they are distinguished on the basis of the velocity boundary conditions applied on the North Atlantic Ridge. Specifically, these conditions are (a) 0, (b) 1/20, and (c) 1/4 of the full spreading velocity given by the NUVEL-1A model at each point on the ridge. These models are labeled 1–3, respectively, in Table 1.

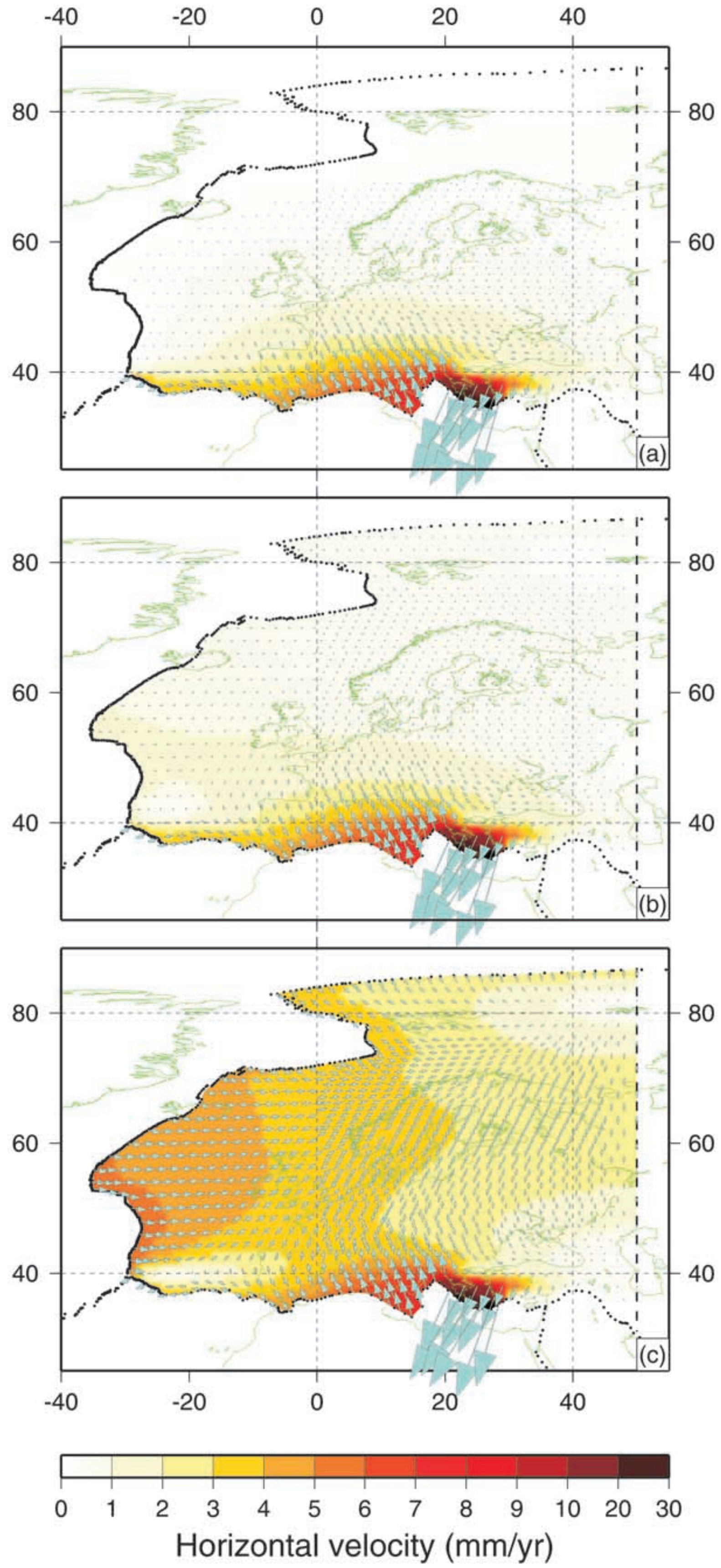

-40
-20
0
20
40
80
60
40
(a)
(b)
(c)
0
1
2
3
4
5
6
7
8
9
10
20
30
Horizontal velocity (mm/yr)

domain; an increase from 0.2 to 0.5 mm/yr is obtained at the latitude of Fennoscandia.

[27] When the velocity along the Atlantic Ridge is increased to 5 mm/yr (leading to an upper bound on ridge push forces, as described in section 1) (Figure 2c), the tectonic velocity in England and Fennoscandia reach magnitudes of ~3 to ~2 mm/yr, respectively. In this prediction the imprint of both the western and southern boundary forcing are clearly evident in the tectonic velocity field. Indeed, along the Alpine Front, north directed motions up to ~4 mm/yr are predicted in Figure 2c, and to the north of this region, sites in central Europe are now characterized by an eastern component of motion.

[28] The velocity patterns shown in Figure 2 represent the intraplate deformation predicted in the case of homogeneous viscosity models and the magnitudes achieved when ridge push forces are large (Figure 2c) do not, in this case, appear to be realistic.

[29] Next, we explore the effect of incorporating lateral variations in lithospheric stiffness into the tectonic model. Figures 3a and 3b show the model predictions when a viscosity increase of two orders of magnitude in the East European subdomain with respect to the reference viscosity (10^{25} Pa s) is taken into account. The two runs are distinguished on the basis of the velocity boundary condition applied along the North Atlantic Ridge, either 0.0 mm/yr (Figure 3a, model 4) or 5 mm/yr (Figure 3b, model 5).

[30] Stiffening of the lithosphere within the East European Platform has the most pronounced effect on predicted tectonic velocities within that region. Specifically, pronounced velocity gradients as one moves north to south across the platform in Figure 2a are reduced considerably in Figure 3a. The net result is a nearly constant crustal velocity of ~0.6 mm/yr across a large portion of the stiffened craton, including Fennoscandia (Figure 3a). The direction of the velocity is also altered (we return to this point in Figure 4a).

[31] The stiffened lithosphere acts to shield the Baltic region and Fennoscandia from the westward directed velocity driven by the ridge and induces a further reduction of gradients in the tectonic velocity field within a stiffened East European Platform (Figure 2c, model 3, compared to Figure 3b, model 5). As an example, consider a profile from 0°E to 40°E along 50°N latitude: with respect to Figure 2c the velocity is reduced in Figure 3b from 3–4 mm/yr to 2–3 mm/yr between 0° and 10°E longitude and from 2–3 mm/yr to 1–2 mm/yr between 10° and 40°E longitude. Stiffening of the East European Platform thus results into a reduced velocity within northern Europe and Fennoscandia even if a significant velocity boundary condition is applied along the North Atlantic Ridge.

[32] Models 6 and 7 are defined by a one order of magnitude reduction of the viscosity within the Mediterranean lithosphere (Figures 3c and 3d, respectively). A comparison of Figures 3c and 2a, for example, indicates that a large amount of the deformation driven by the boundary conditions to the south takes place in the weakened lithosphere; this results in velocity gradients being significantly localized to the Mediterranean. Note that the relatively small velocities within Fennoscandia in Figure 2a extend well south into central Europe in Figure 3c (see also the detail of Figure 3c given in Figure 4b). Clearly, intraplate deformation in Europe due to Africa-Eurasia convergence is sensitive to the amount of deformation which takes place within the Mediterranean lithosphere.

[33] Model 7 introduces a velocity along the North Atlantic Ridge into the simulation characterized by a weakened Mediterranean lithosphere, and the result (Figure 3d) can be compared to Figure 2c. Clearly, weakening the Mediterranean subdomain allows the eastward directed velocity driven by the Atlantic spreading to extend more deeply into Europe. Note, for example, the dramatic eastward migration of the 4 mm/yr contour in Figure 3d relative to Figure 2c.

[34] Figure 4a provides a detail of the model 4 predictions within the East European Platform. Stiffening the lithosphere in this region has resulted into a broad motion of the platform toward the southwest, that is toward the lithospheric (European, Mediterranean) subdomains of lower viscosity. Figure 4b is an enlargement of the model 6 result. Relative to a model with the stiffened East European Platform (Figure 3c), lowering the viscosity in the Mediterranean subdomain has the effect of inverting the predicted direction of motion in Fennoscandia from SW to NE with respect to Figure 4a and reducing the magnitude of the velocity from 0.8–1.0 to 0.2–0.3 mm/yr in the same region.

[35] The results in Figures 1–4 indicate that the amplitude and direction of predicted horizontal velocities at sites located well away from plate boundaries are sensitive to the adopted modeling parameters. As an example of the latter, consider Fennoscandia. Varying of model parameters above led to a suite of predictions for this region (e.g., see Figure 4). It is interesting to note, in this regard, that a number of these predictions yield amplitudes comparable to the "residuals" obtained by subtracting best fit GIA predictions from GPS-determined horizontal crustal velocities [see *Milne et al.*, 2001, Figure 6b]. We return to each of these points in section 5.

4. Sample Model Results: GIA-Induced 3-D Crustal Velocity

[36] The 3-D velocity fields predicted by models of GIA have shown relatively consistent patterns [*James and Lambert*, 1993; *Mitrovica et al.*, 1993, 1994b; *Peltier*, 1998], and the general forms of these predictions were confirmed by comparison with results from the dense GPS network BIFROST [*Johansson et al.*, 2002; *Milne et al.*, 2001].

[37] As an illustration of the expected patterns of GIA, in Figure 5 we show maps of present-day radial and horizontal crustal velocities predicted using the GIA model summarized in section 2 (model 8, Table 1). As discussed above, the ice and Earth model combination adopted in the model was shown by *Milne et al.*, [2001] to provide an excellent fit to the BIFROST observations. Figure 5 shows the geometry of 3-D crustal adjustment over the region considered in Figures 1–4 and is thus an extension of *Milne et al.* [2001, Figure 3] plots which were limited to Fennoscandia. Figure 5a is characterized by radial uplift reaching ~11 mm/yr over Fennoscandia and subsidence of several millimeters per year within a peripheral bulge that extends, for example, well into central Europe.

[38] Horizontal motions are directed outward from the center of deglaciation, and are close to zero at this center, eventually reaching a maximum amplitude (~6 mm/yr) near

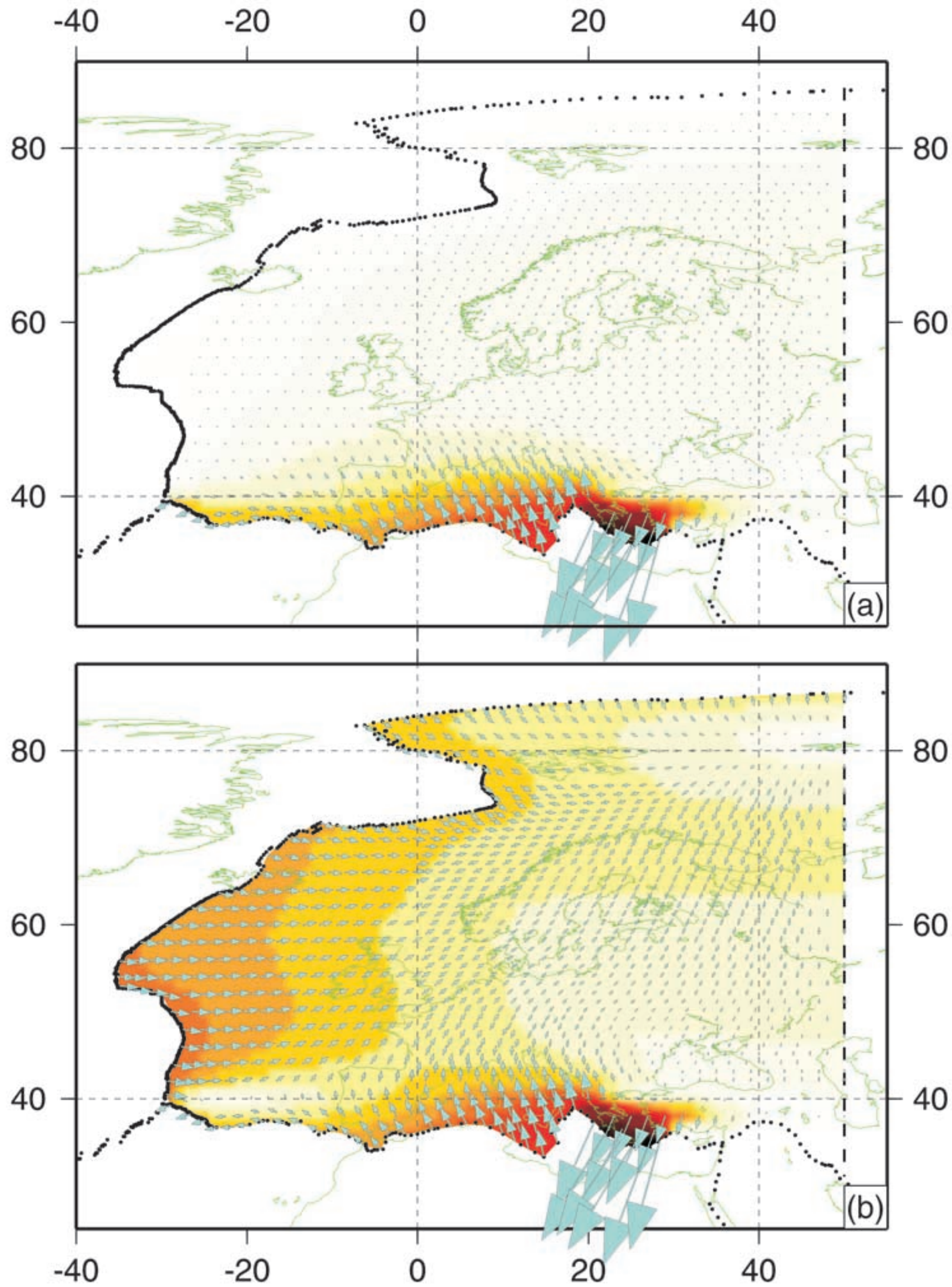

Figure 3. Same as Figure 2, except for models 4–7 of Table 1, respectively. In particular, (a) and (b) Models in which the East European Platform is 2 orders of magnitude stiffer then the reference European subdomain (models 4 and 5, respectively). (c) and (d) Viscosity of the Mediterranean subdomain, which is reduced by 1 order of magnitude relative to the reference value of the European subdomain (models 6 and 7, respectively). Furthermore, these models sample cases in which the velocity condition applied along the North Atlantic Ridge (in order to model ridge push forces) is either zero (Figures 3a and 3c) or 1/4 (Figures 3b and 3d) of the NUVEL-1A full spreading velocities, ~0.0 or 5.0 mm/yr, respectively.

the location of the northwestern edge of the ice sheet at the Last Glacial Maximum (LGM). At further distance, the amplitude of the horizontal motions diminishes until a pattern of inward directed (i.e., toward the ancient Fenno-scandian ice complex) horizontal motions emerge. GIA-induced horizontal motions due to the unloading of Fennoscandian ice are more symmetric about the center of deglaciation than the patterns in Figure 5. The asymmetry in the horizontal motions in Figure 5 (amplitudes of the outward motions are higher in the northwest than the southeast) is due to a combination of rotational effects and the far-field adjustment due to unloading of Laurentia

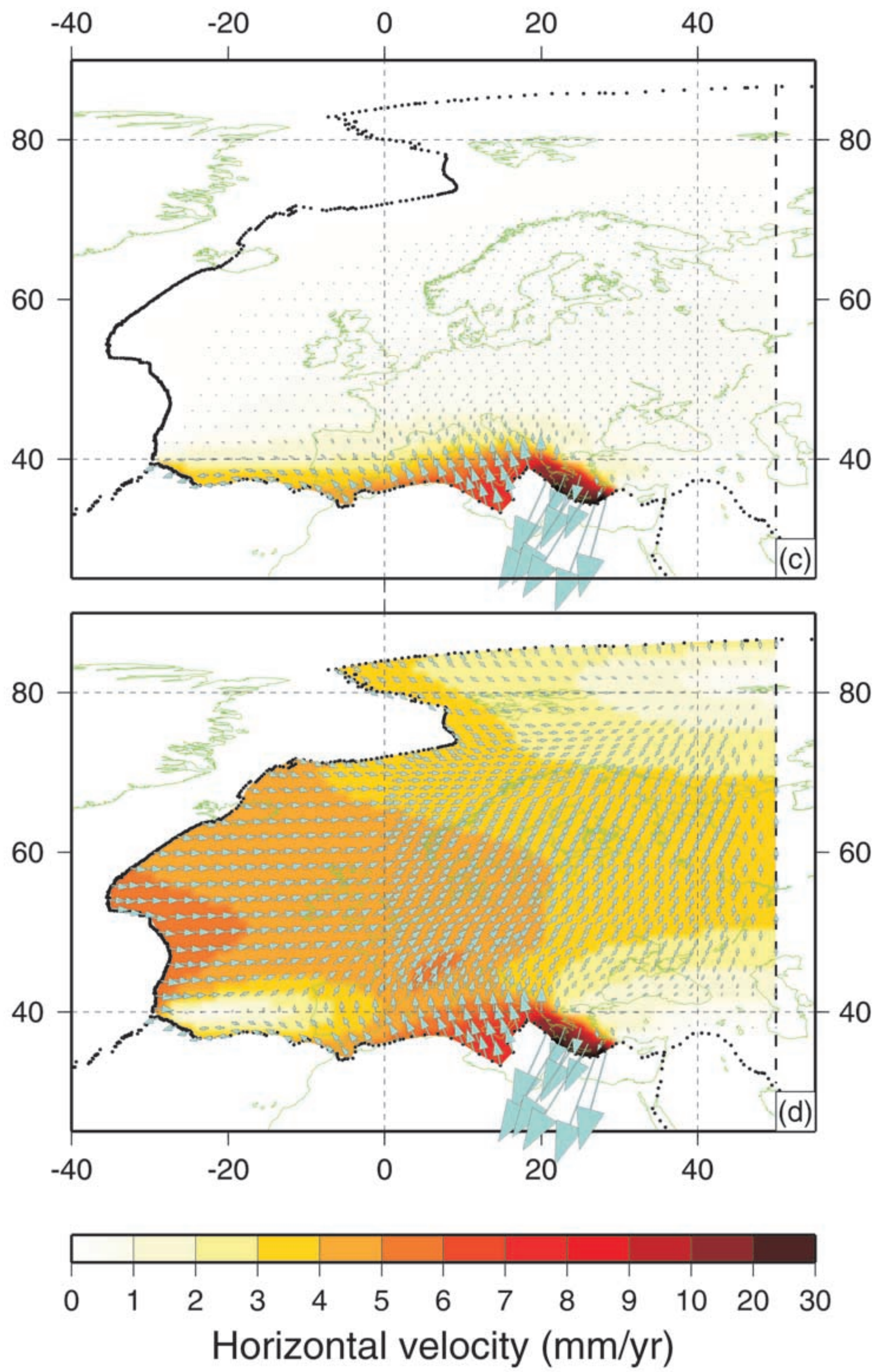

Figure 3. (continued)

(which is characterized by motions in the northwest direction toward Laurentia) [*Milne et al.*, 2001].

5. Baseline Rates: ITRF2000-BIFROST Data and Sites

[39] In this section we compare our tectonic and GIA predictions to the GPS data available for the study domain. For this purpose we compare predicted and observed values of baseline rates (i.e., length changes) for baselines defined with respect to three reference sites: POTS (Potsdam, Germany); ONSA (Onsala, Sweden), and VAAS (Vaas, Finland).

[40] These sites are expected to have varying levels of deformation associated with tectonic and GIA processes. As suggested by the predictions shown in Figures 1–4, tectonic

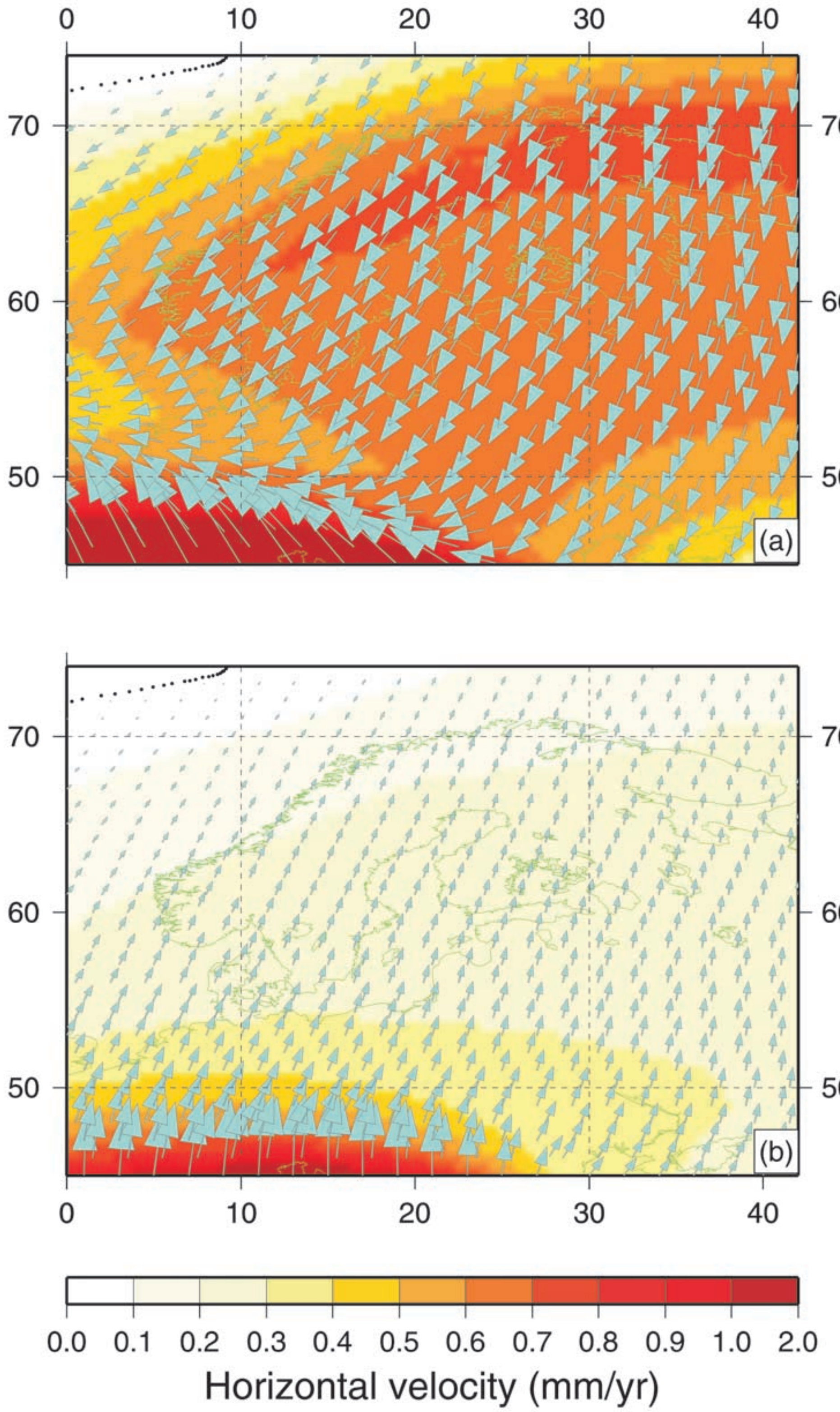

Figure 4. Details of the velocity predictions for (a) model 4 and (b) model 6.

velocities associated with boundary forcing at the African-Eurasia-Aegean plate contact tend to decrease as one moves northward (POTS, ONSA, VAAS), although forcing from the spreading along the Atlantic Ridge clearly complicates this simple geometry. Since VAAS lies near the center of the Fennoscandian ice complex at its greatest extent, the GIA-induced radial motions are near a maximum, while the associated horizontal motions are relatively close to zero.

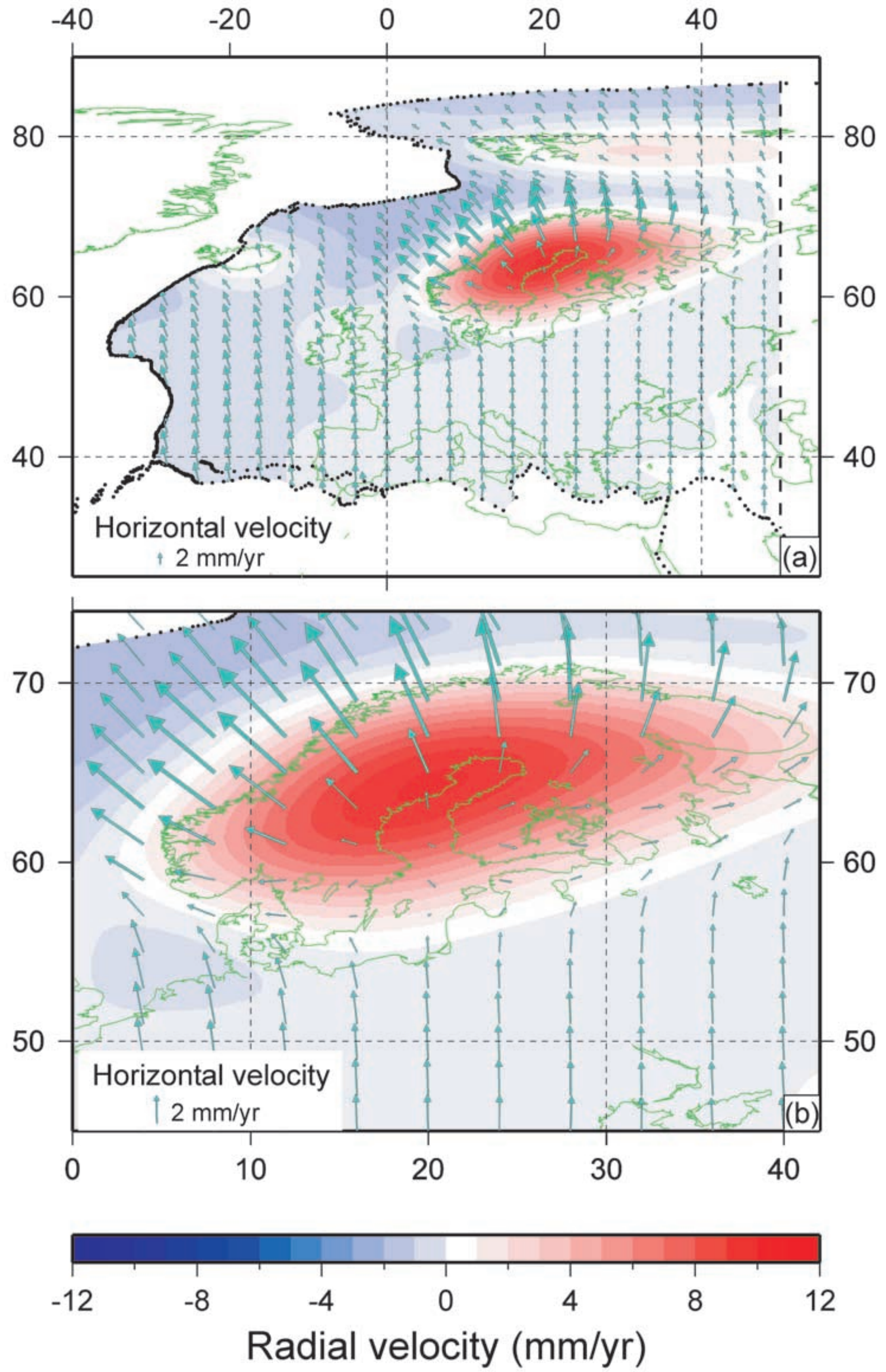

Figure 5. Maps showing radial (colors) and horizontal (arrows) crustal velocity predicted by the GIA model (model 8, Table 1) described in detail in the text. (a) Global view. (b) Enlargement of the Fennoscandia region.

(Choosing VAAS as a reference site also has the advantage that it appears in both the BIFROST and ITRF2000 databases.) The ratio of horizontal to radial GIA motions increases as we move from VAAS to POTS. ONSA is near the edge of the Fennoscandian ice sheet at LGM; the predicted radial motion is ~3 mm/yr versus a horizontal velocity of ~1.5 mm/yr. POTS, which lies on the peripheral bulge of the GIA-induced crustal motion, is characterized by predicted radial and horizontal motions of ~−1 and ~2.5 mm/yr, respectively.

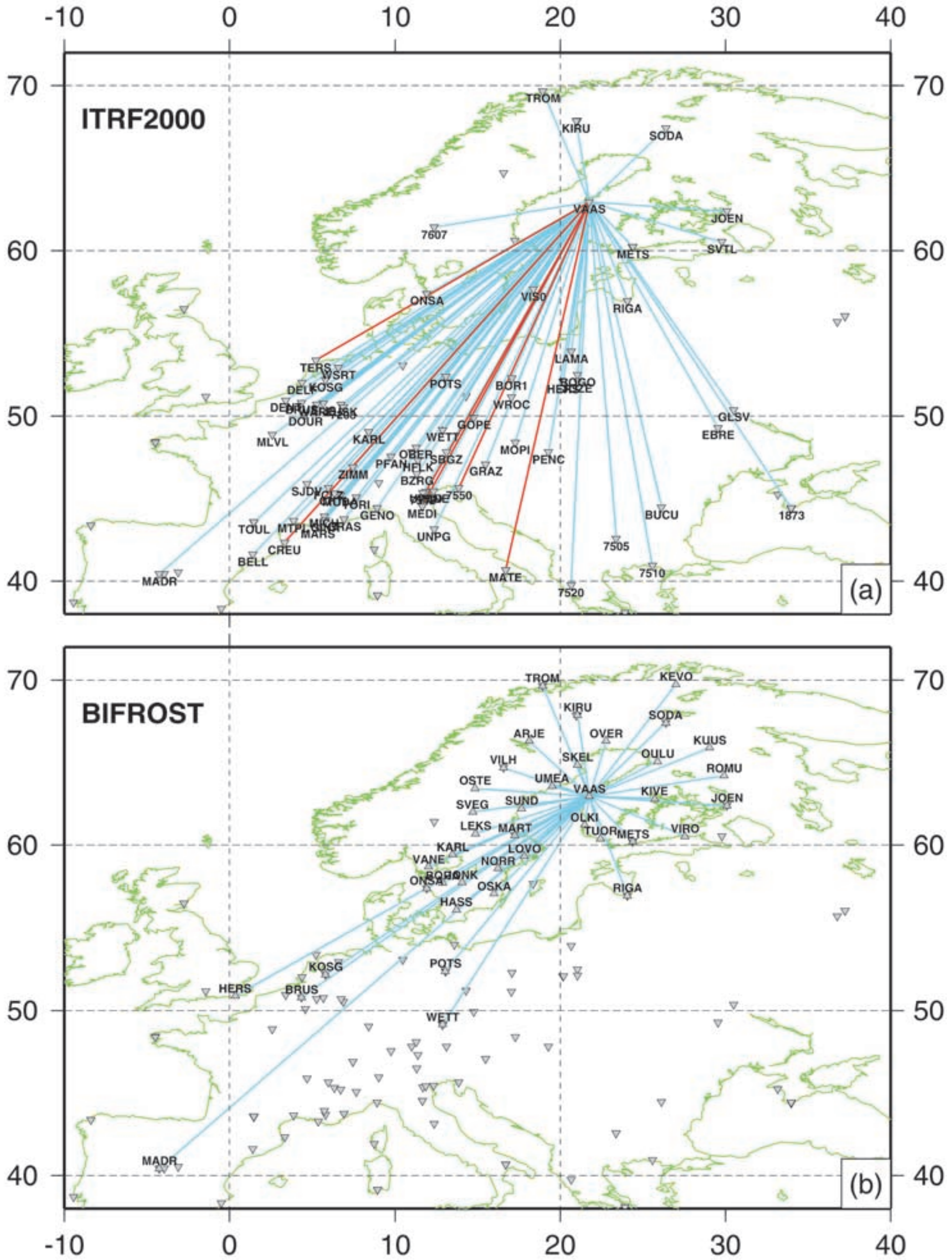

Figure 6. Observed baseline rates for baselines referenced to the site VAAS, where blue indicates extension and red shortening, according to (a) ITRF2000 and (b) BIFROST data sets. Grey inverted triangles indicate the ITRF2000 sites while triangles indicate BIFROST sites.

[41] The baseline rate, BL, is formally given by

$$\frac{\partial(\mathrm{BL})}{\partial t} = (\mathbf{V}_1 - \mathbf{V}_2) \cdot \frac{(\mathbf{r}_1 - \mathbf{r}_2)}{|\mathbf{r}_1 - \mathbf{r}_2|} \tag{14}$$

which defines a projection of relative velocity between sites 1 and 2, $(\mathbf{V}_1 - \mathbf{V}_2)$, onto a unit vector in the direction of the baseline vector extending from site 1 to site 2, $((\mathbf{r}_1 - \mathbf{r}_2)/|\mathbf{r}_1 - \mathbf{r}_2|)$. As discussed in section 2, our thin sheet tectonic model yields predictions of horizontal motion only, and thus in this case the baseline rates are predicted on the basis of this component. This limitation should not introduce significant errors since the applied tectonic forcings would not be expected to produce large vertical velocities at the European sites. In contrast to this aspect of the modeling, the GIA baseline predictions are based on a 3-D response theory, reflecting the significant vertical and horizontal contributions to the velocity field induced by ice-ocean surface mass loading.

[42] To begin, we consider the observed baseline rates with respect to the reference site VAAS. Figures 6a and 6b show the location of baselines associated with ITRF2000 and BIFROST data sets, respectively, where the observed dominant extension is denoted by blue and the observed shortening by red. The sites in Figure 6 listed as BIFROST sites include, in addition to sites in the actual BIFROST

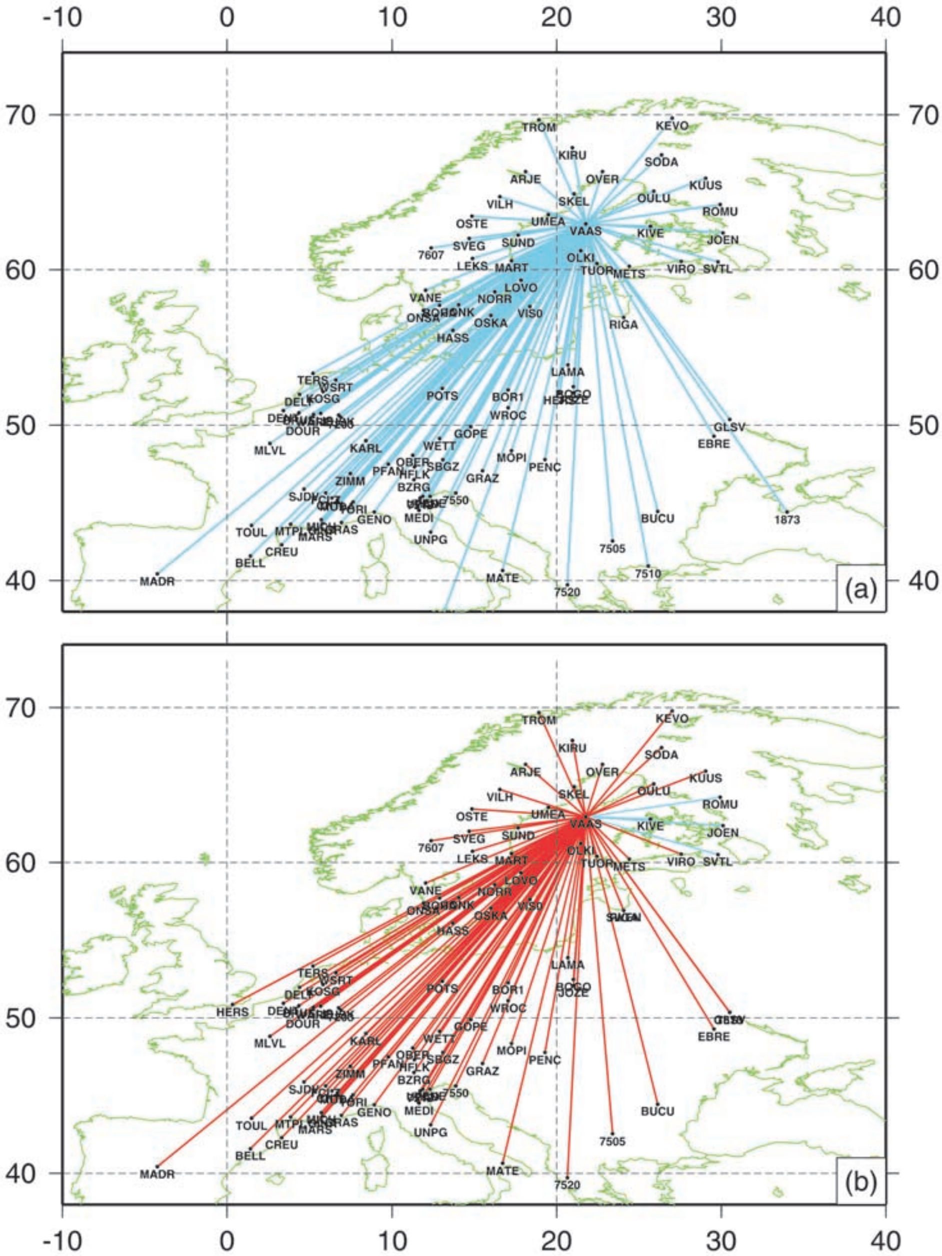

Figure 7. Predicted baseline rates for baselines referenced to the site VAAS, where blue indicates extension and red shortening for (a) model 8, (b) model 1, (c) model 5, and (d) model 7.

network, a set of five other sites (HERS, MADR, BRUS, KOSG, POTS, WETT, RIGA) that were included in crustal velocity solutions published on the BIFROST Web site (http://www.oso.chalmers.se/~hgs/Bifrost_01/index.html). We will henceforth refer to all these sites as "BIFROST sites," but the reader should be aware of the distinction.

[43] Figure 7a shows our GIA prediction (as in Figure 5) of the sign of the baseline rate for all the VAAS-referenced baselines in Figure 6. Except for some inconsistencies with a few southerly directed baselines, the GIA model captures the major feature of Figure 6, namely, the dominant extension in the ITRF2000 and BIFROST data.

[44] Since postglacial adjustment in Fennoscandia is characterized by horizontal motions directed outward from the center of the ancient ice complex (i.e., near VAAS), widespread extension along the short BIFROST baselines (Figure 6b) is expected. The origin of the widespread extension for the longer ITRF2000 or BIFROST baselines extending to central and southern Europe (Figures 6a and 6b), and in particular the role of GIA in this pattern, is less obvious. To explore this issue, consider again Figure 5. As described above, the horizontal velocity field is characterized by outward directed motions within Fennoscandia, changing to motions toward Fennoscandia at the periphery. On the basis of this prediction, one might expect that GIA would induce shortening in the longer (VAAS to central/southern Europe) baselines within Figure 6a. However, as it is clear from equation (13), both horizontal and radial

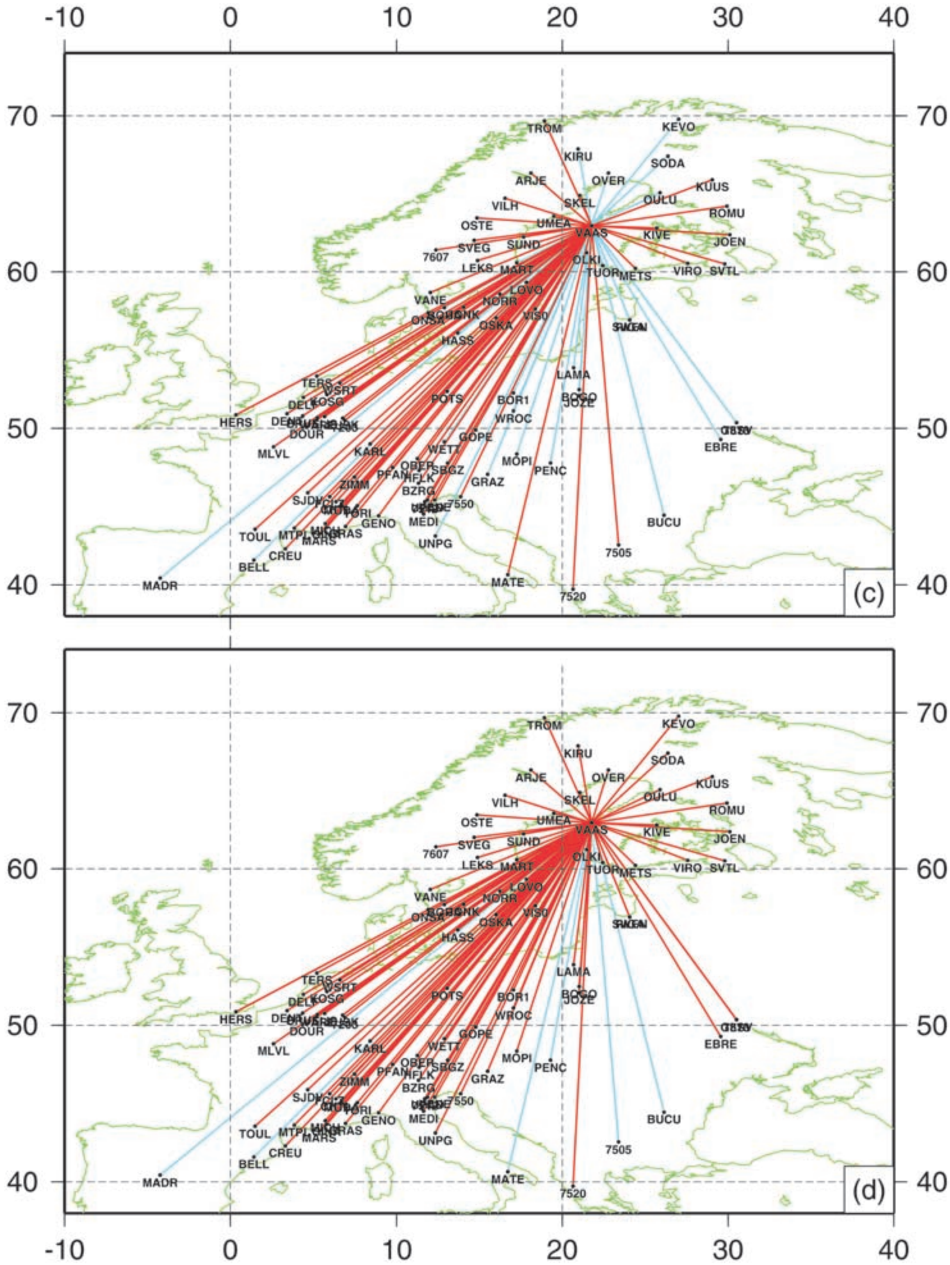

Figure 7. (continued)

motions contribute to these rates. From Figure 5, VAAS is predicted to be uplifting at a rate close to 1 cm/yr, while central and southern European sites, which lie within the peripheral bulge of Fennoscandia, are subsiding at lower rates. The net contribution of this uplift and (more moderate) subsidence is to extend the baselines. Indeed, this signal is sufficient to counter the baseline shortening associated with the GIA-induced horizontal velocity field and the net result is consistent with the pattern of widespread extension evident in the longer baselines in Figure 6a. Of course, these arguments refer primarily to the net sign of the GIA-induced baseline rate, rather than the amplitude, and we explore the latter in detail in Figure 8.

[45] Figures 7b–7d show predictions of baseline rates generated from a subset of our tectonic models. Figure 7b summarizes results based on model 1 (Table 1), characterized by a homogeneous lithosphere, Africa-Eurasia convergence, and no Atlantic Ridge forcing. In this case the VAAS-referenced baselines show a general pattern of shortening, except for a limited extension for short baselines connecting three sites east of VAAS. Except for this extension, the style of baseline rates is opposite to the observed pattern.

[46] This sequence of predictions is completed in Figures 7c and 7d, where we summarize results for models in which lateral variations in plate strength are introduced (models 5 and 7, respectively). With respect to the predictions of the homogeneous model (model 1, Figure 7b), model 5 (Figure 7c) improves the fit to the observed baseline rate pattern by yielding extension for

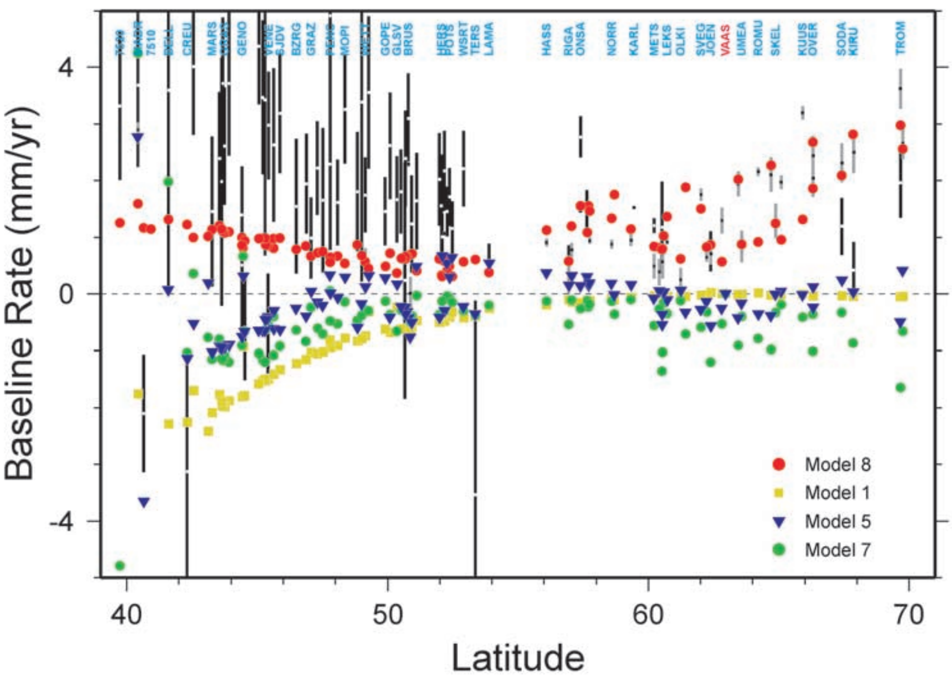

Figure 8. Amplitudes of the predicted baseline rates, with respect to VAAS, for the baselines shown in Figures 7a–7d, for model 8 (red dots), model 1 (yellow dots), model 5 (blue triangles), and model 7 (green dots), compared to the observed values of baseline rates (black vertical bars correspond to ITRF2000, and grey vertical bars correspond to BIFROST data sets).

baselines directed from southeast to south-southwest; however, the model predicts shortening for other baselines, contrary to the observations. The results in Figure 7d for model 7 are broadly similar in form to model 5 predictions, except for a further reduction in extension, for both northerly and southerly directed baselines.

[47] The amplitudes of the observed and predicted VAAS-referenced baseline rates are compared in Figure 8, where constraints provided by the ITRF2000 and BIFROST observations are denoted by the black and grey vertical bars, respectively. The baselines in Figure 8 are ordered on the basis of the latitude of the second site defining the baseline (the first being VAAS), and for clarity, only a subset of these are named at the top of the frame. (Note that the uncertainties associated with the BIFROST data are significantly smaller, on average, than the uncertainty in baseline rates determined from the ITRF2000 database.)

[48] The red dots on the frame refer to the numerical GIA predictions (i.e., the velocity fields of Figure 5 applied to equation (13)). Note, first, the excellent fit of the numerical GIA predictions to the well-constrained rates for baselines within Fennoscandia. This fit is not surprising given that the ice/Earth model combination used in the numerical prediction was found by *Milne et al.* [2001] to "best fit" the BIFROST-determined 3-D crustal motions. It is also clear from the pattern of the red dots for latitudes south of 52°, that the same numerical model, while yielding a pattern of extension for baselines ending at central and southern European sites (see also Figure 7a and the discussion above concerning the origin of this extension), does not appear to reconcile the observed amplitude of this extension. Indeed, the baseline rates determined from ITRF2000 data are perhaps a factor of 2–3 larger than the values predicted by the GIA model alone.

[49] What is the source of the residual extension evident in the VAAS to central/southern European baselines in Figure 8? One possibility is that the observed VAAS site velocity is in error. A second possibility is that the GIA model is in error, perhaps because of errors in the adopted ice history and radially stratified viscoelastic structure. While there is certainly leeway in these models, any alternative combination of these inputs must be constrained to provide a comparable fit to the BIFROST data. To partly explore this issue, we repeated the calculations in Figure 8 for a series of Earth models in which either the lithospheric thickness, upper mantle viscosity, or lower mantle viscosity was varied from the values defining the *Milne et al.* [2001] best fit case. These ranges, guided by the χ^2 misfit analysis presented by *Milne et al.* [2001], were 96–146 km, 0.5–1.0 $\times$ 10^{21} Pa s, and 5–20 $\times$ 10^{21} Pa s, respectively. None of these GIA models produced a VAAS-to-central/southern European baseline extension significantly larger than that evident in Figure 8. In future work we will explore, in detail, this insensitivity and extend the analysis to a more complete range of Earth model and ice history cases.

[50] The other possibility is that the residual signal evident in Figure 8 for GIA originates from tectonic forcing. Our tectonic predictions are given by the yellow squares (mode 1), blue triangles (model 5), and green dots (model 7).

[51] Model 1 predicts a shortening that tends to increase as one moves toward the southern plate boundary, between 40° and 50°N. This result is easily understood in terms of the velocity pattern in Figure 2a driven primarily by the

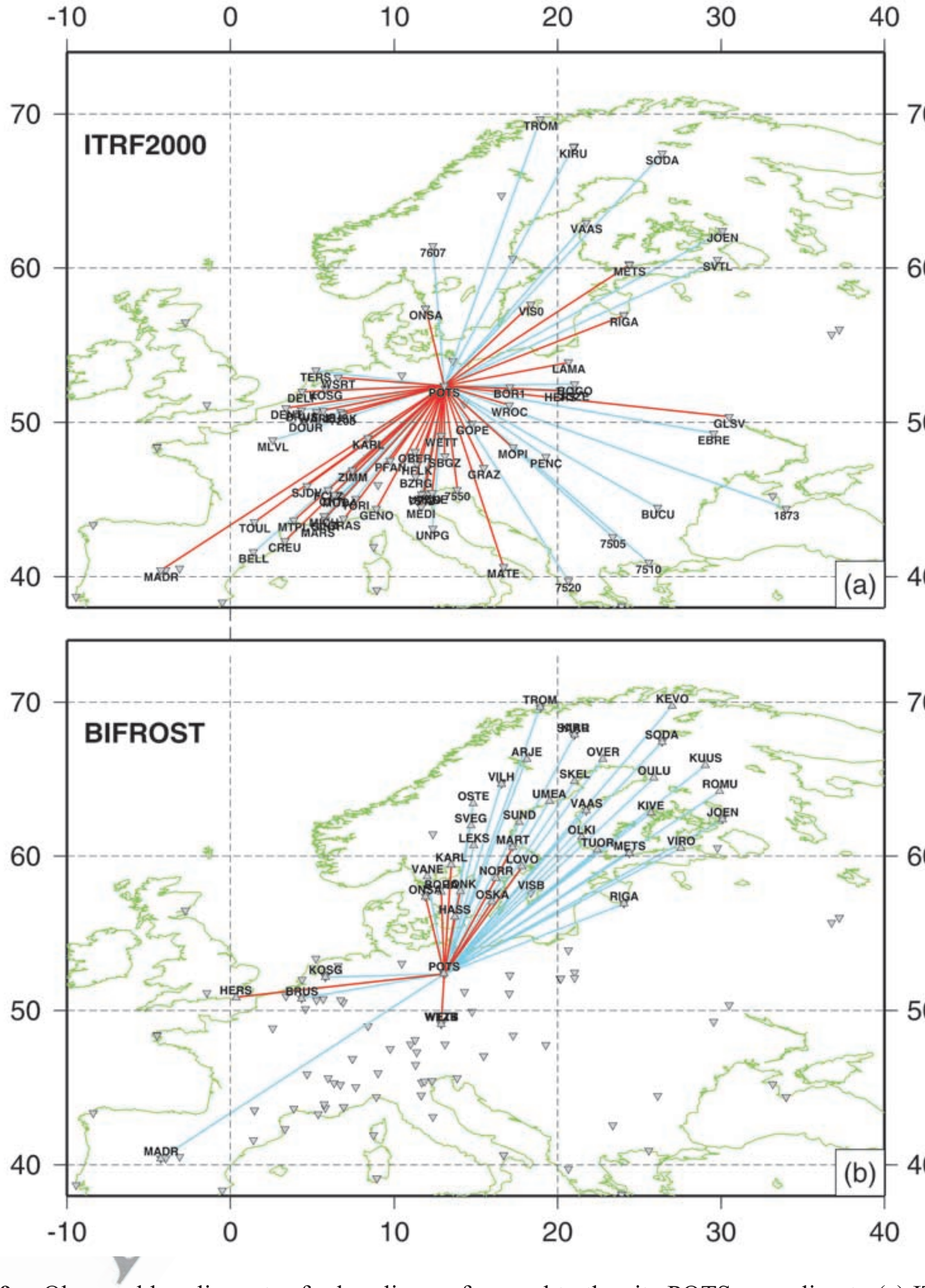

Figure 9. Observed baseline rates for baselines referenced to the site POTS according to (a) ITRF2000 and (b) BIFROST data sets. Grey inverted triangles indicate the ITRF2000 sites, while triangles indicate BIFROST sites.

Africa indenter. Note that the extension evident for baselines ending at sites east of VAAS (Figure 7b) is of insignificantly small amplitude. We can conclude that this tectonic model does not impact the GIA fit to the BIFROST baselines and adds to the residual associated with the longer baselines.

[52] The tectonic model 5 yields some extension in baselines ending at sites close to 50°N; however, it is unable to explain the dominance of extension in the observations for baselines extending from VAAS to sites between 40° and 46°. North of 50°N, this model predicts some limited extension and shortening but of amplitude insufficient to corrupt the GIA results. The results for model 7 are broadly similar to model 5 predictions in form, but they tend to be displaced downward in the diagram; thus shortening instead of extension is predicted for all baselines ending at sites with latitudes higher than 56°N.

[53] In Figure 9 we turn our attention to baselines referenced to the Potsdam site (POTS) in northern Europe. Short BIFROST baselines defined by sites between 55° and 60°N are primarily in compression, while baselines extending to more northerly sites are in extension (Figure 9b). The same pattern is evident in the ITRF2000 baselines extending into Fennoscandia (Figure 9a). The ITRF2000 baselines within northern, central and southern Europe are characterized by variable style. These baselines are predominantly in

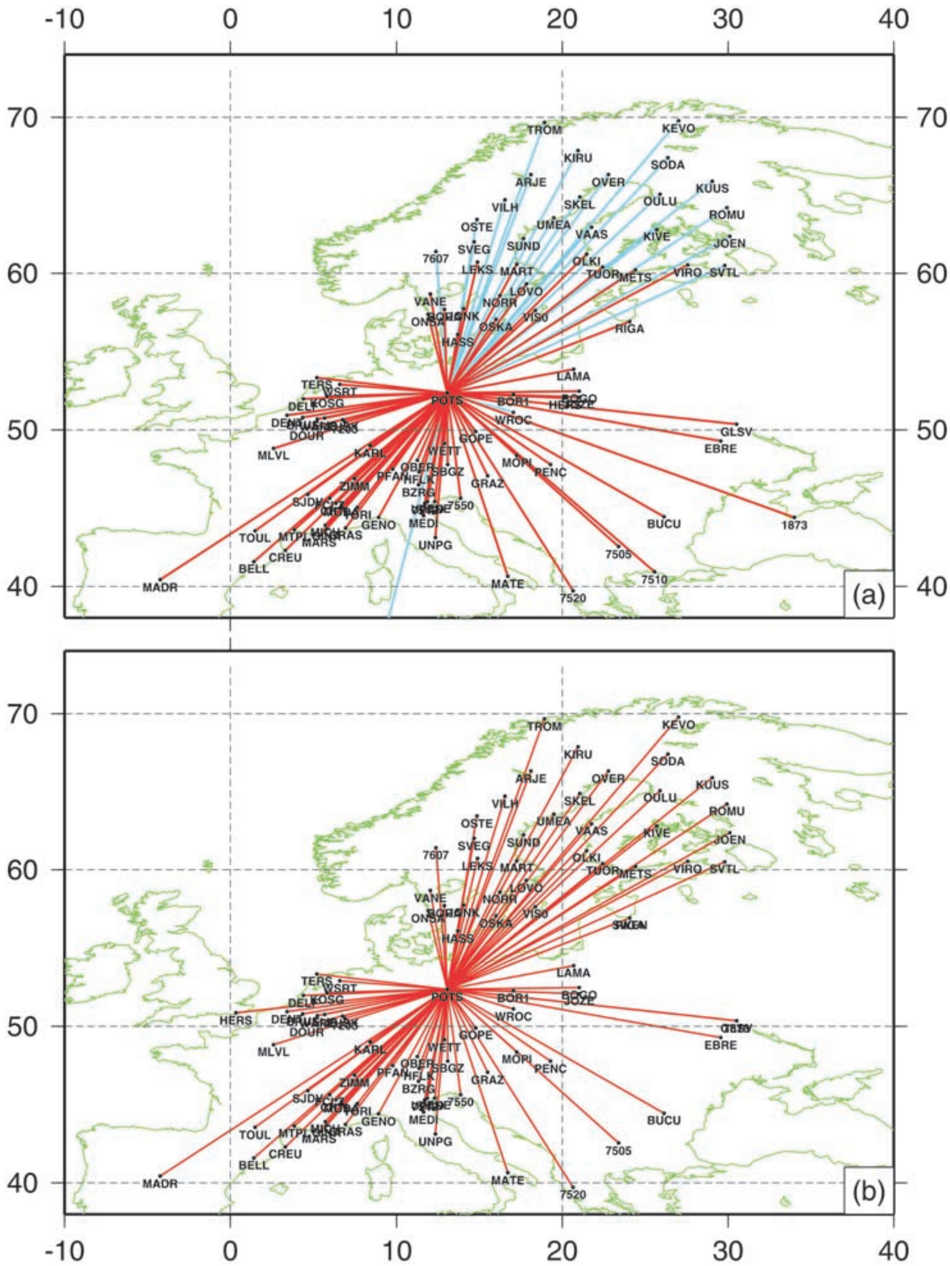

Figure 10. Predicted baseline rates for baselines referenced to the site POTS for (a) model 8, (b) model 1, (c) model 5, and (d) model 7.

compression; however, a number of them show extension, for example, a cluster of baselines defined by sites in the southeast portion of Figure 9a.

[54] Figure 10a shows predictions for the same set of baselines generated using the GIA model described above (model 8, Table 1). This model reconciles the pattern evident in the northern baselines, in particular, a transition from shortening to extension as one considers more northerly sites.

[55] In Figures 10b–10d we show POTS-referenced baseline results generated by using the same three models used to construct Figures 7b–7d, respectively.

[56] The uniform lithosphere model 1 (Figure 10b) is driven by forcing along the southern (Africa-Eurasia) boundary and the resulting northward decrease in velocity (Figure 2a) yields a shortening of all baselines, thus failing to reproduce the extension of the baselines connecting sites north of POTS.

[57] Figure 10c illustrates the impact on the POTS-referenced baselines of stiffening the East European Platform (model 5). The combined effect of a viscosity increase in the Baltic Shield and a push from the Atlantic Ridge reproduces the observed pattern of dominant shortening between POTS and the Mediterranean and extension between POTS and Fennoscandia. In reference to Figure 3b, the effect of the shield is to maintain into southern and central Europe the north directed motion driven by the Africa indenter. The stronger platform acts to significantly reduce

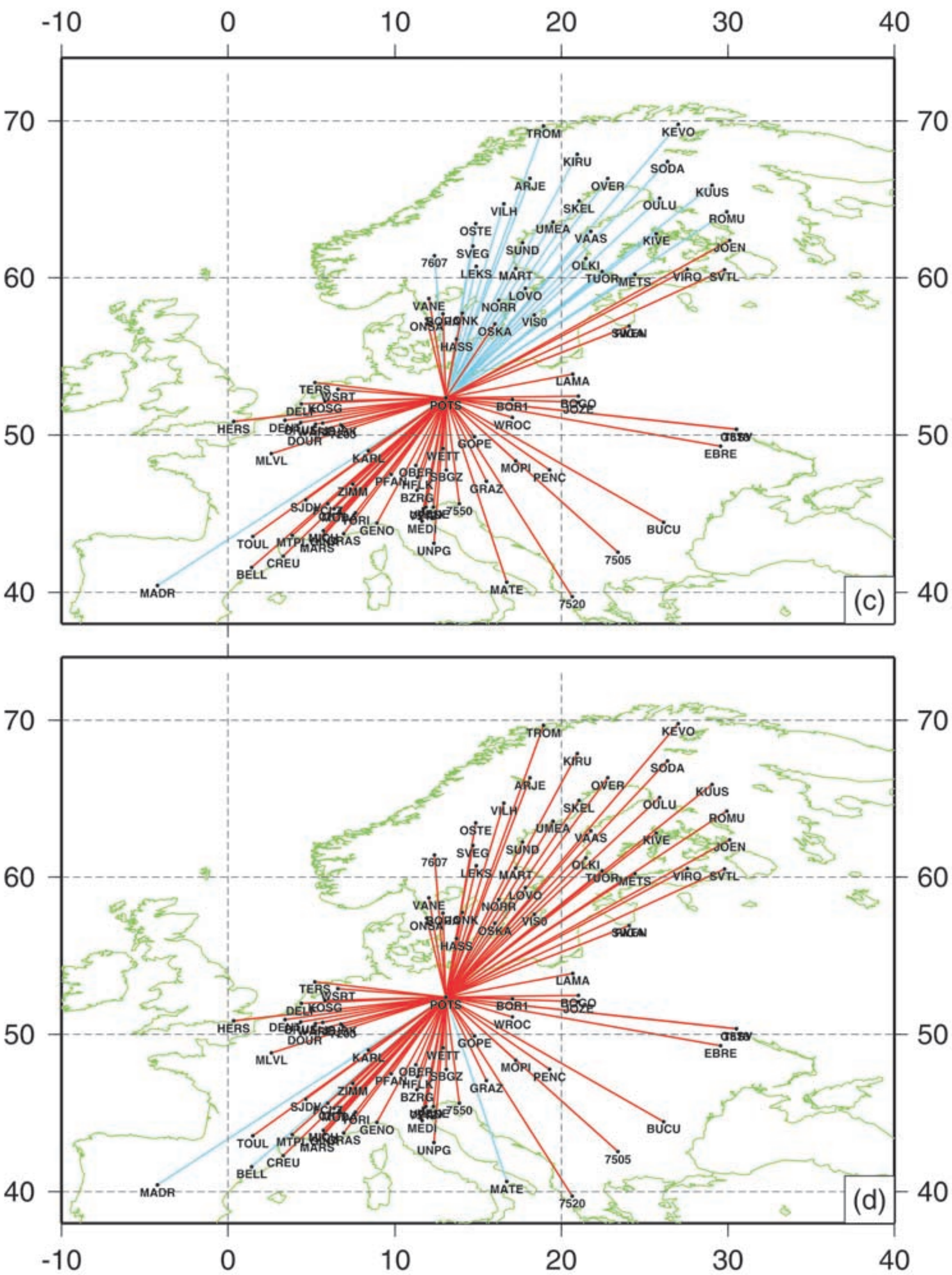

Figure 10. (continued)

the predicted tectonic deformation across central and northern Europe, including Potsdam (compare Figures 2d and 3b). As a consequence, sites clustered near the Africa-Europe plate boundary in the southwest (latitudes 43° and 48°N) are predicted to move toward a relatively more stationary Potsdam, and the result is a predicted shortening of these baselines. Figure 10c thus shows that a realistic tectonic model characterized by a stiffening of the lithosphere in the Baltic Shield and a velocity applied along the Atlantic Ridge which simulates ridge push forces can reproduce the dominant shortening of baselines from POTS south and contributes to the extension north of this site.

[58] For the final tectonic model of this sequence (model 7, Figure 10d) the weakened Mediterranean subdomain, in contrast to the strong Baltic Shield case, leads to a decrease in horizontal motions as one moves north from POTS through the Fennoscandian region (Figure 3d). As a consequence, this model predicts shortening of baselines ending with BIFROST sites.

[59] In Figure 11 a comparison between the amplitude of the observed and predicted baseline rates is shown for baselines referenced to POTS.

[60] The observed shortening of baselines ending at sites within 56°–60°N appears to be somewhat overestimated by the GIA model (red dots). For baselines ending with sites at Potsdam's latitude or below, the GIA model predicts a low amplitude shortening, which is a consequence of both the horizontal and radial motion patterns in Figure 5. The GIA

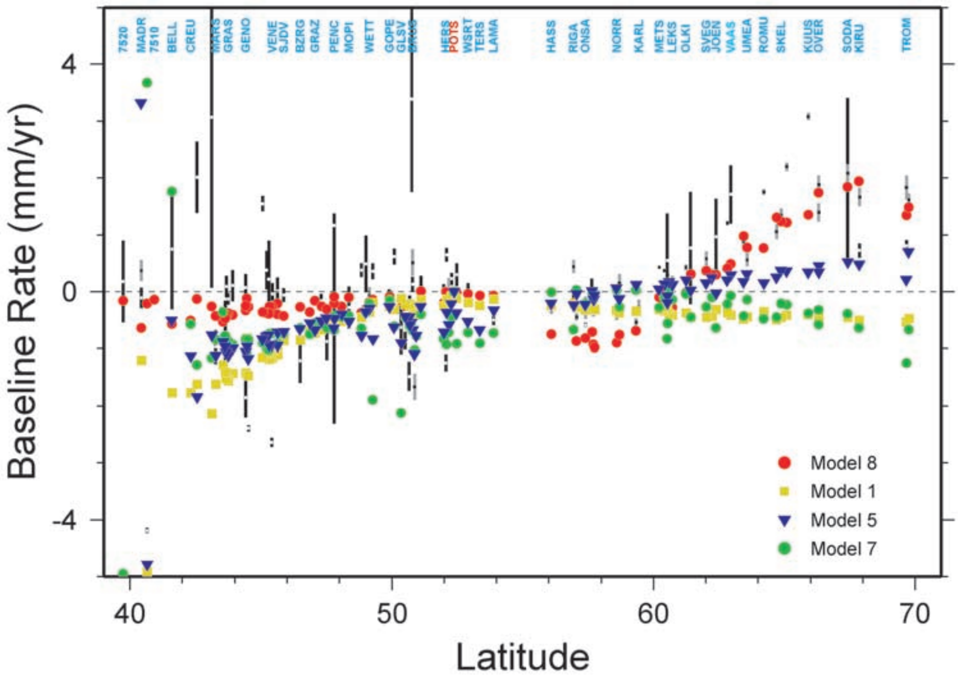

Figure 11. Amplitudes of the predicted baseline rates, with respect to POTS, for the baselines shown in Figures 10a–10d, for model 8 (red dots), model 1 (yellow dots), model 5 (blue triangles), and model 7 (green dots), compared to the observed values of baseline rates (black and grey vertical bars have the same significance of Figure 8).

pattern is broadly consistent with the observed rates, although discrepancies for individual baselines can be large.

[61] Model 1 (yellow squares) predicts a shortening of baselines ending in proximity to the southern boundary; this shortening decreases as one moves to latitudes close to that of the reference site POTS (50°–55°N) and then increases again (to up to 0.5 mm/yr) as one moves northward through the BIFROST baselines. Note that the baselines in the latitude range 50°–55°N are oriented at roughly \right angles to the tectonic velocity field (Figure 2a) and this accounts for the relatively insignificant rates predicted for these baselines.

[62] The tectonic model 5 (blue triangles) predicts a shortening of all baselines ending at sites below 60°N (see also Figure 10c). As a consequence of the stronger platform, the forcing at the southern boundary is reduced north to Fennoscandia and the result, relative to the POTS site, is an extension of such baselines north of 60°N. We note that model 5 yields a rather good fit to the POTS baselines for sites within the range 46°–60°N. The model also yields a moderate (fraction of a millimeter per year) extension in the baselines ending at the more northern BIFROST sites. The weakened Mediterranean subdomain (model 7, green dots), in contrast to the strong Baltic Shield case, leads to shortening of comparable amplitude to that predicted by model 5 for sites south of Potsdam. Model 7 predicts a shortening, instead of the extension evident in the model 5 results for sites north of Potsdam.

[63] Finally, Figure 12 compares predictions with observations for baselines referenced to ONSA. Both observations and model predictions suggest patterns similar to those of Figure 11. The GIA model simultaneously reconciles the tendency for shortening on baselines ending south of ONSA and the extension in the (northern) BIFROST baselines. Model 1 yields shortening for baselines ending at sites between 40° and 50°N. The behavior of model 5 is similar to the Figure 11 results, except for some scattered shortening for latitudes north of 60°. Model 7 also predicts a pattern of shortening for ONSA baselines extending to sites south of 52°N. This shortening becomes negligible when sites between 54° and 58°N are considered, while it is of highly variable amplitude when considering baselines ending at sites north of 60°N.

[64] The results shown by Figures 8, 11, and 12 may be summarized by noting that the GIA model performs best for the baselines connecting the three reference sites to sites located north of 58°–60°N. The same conclusion holds for southerly directed baselines when VAAS is the reference site. For the reference sites ONSA and POTS, GIA underestimates the shortening observed for the baselines connecting sites south of about 58°, while the tectonic models generally provide for an improved fit as far as this shortening is concerned. Among the tectonic models, the best performing cases are those characterized by lateral viscosity variations, either in the Baltic Shield or in the Mediterranean subdomains, since in both cases the predicted tectonic shortening does not reach Fennoscandia (and thus does not corrupt the excellent fit obtained by the GIA model in this region).

[65] In section 6 we perform a statistical (χ^2) analysis in an attempt to more robustly quantify the deviation between model predictions and observations and isolate a "best fitting" combination of GIA and tectonic models.

6. The χ^2 Analysis

[66] To complete this study, we perform a χ^2 analysis to determine which of the 19 models in Table 1 best fit the

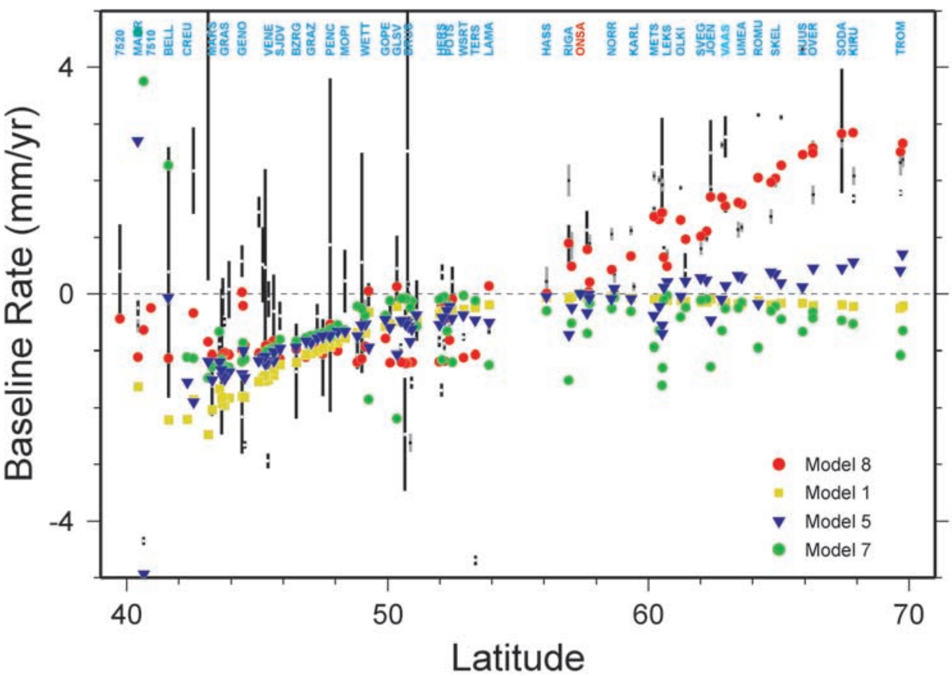

Figure 12. Amplitudes of the predicted baseline rates, with respect to ONSA, for the baselines shown in Figures 7a–7d, for model 8 (red dots), model 1 (yellow dots), model 5 (blue triangles), and model 7 (green dots), compared to the observed values of baseline rates (black and grey vertical bars have the same significance of Figure 8).

observations. For this purpose, we will consider ITRF2000 baselines only; the GIA model 8 was tuned to best fit BIFROST baselines; as we have seen, this procedure yielded small residuals and thus little scope for neotectonic deformations [*Milne et al.*, 2001].

[67] Let us define the usual χ^2 statistic for the performance of the mth model as

$$\chi^2(m) = \sum_{i=1}^{N} \frac{(\mathrm{BR}_{oi} - \mathrm{BR}_{mi})^2}{\sigma_{oi}^2} \qquad (15)$$

where BR_{mi} and BR_{oi} denote the ith component of vectors whose components correspond to the values of the modeled and observed baseline rates, respectively. The variance associated with the ith baseline rate is σ_{oi}^2, and N represents the total number of baselines.

[68] In Figure 13 we plot the χ^2 misfit computed for each of the 19 models in Table 1 for the set of ITRF2000 baselines. It is clear from Figure 13 that model 14, which combines the tectonic model 6 with the GIA model 8, provides the best fit to the observations. As we discussed above, model 6 is characterized by a soft Mediterranean subdomain: this region acts to reduce the impact of tectonic forcing due to Africa-Eurasia convergence at sites north of Potsdam, and thus it preserves the fit to northern baselines achieved by the GIA model. In this regard, we note that the next best χ^2 value is achieved by model 5, which reduces the tectonic deformation for sites north of Potsdam by stiffening the Baltic Shield.

[69] The results in Figure 13 do not represent an exhaustive investigation of model space. However, Figure 13 demonstrates that a combination of tectonic and GIA models has the potential to improve misfits to observed baseline rates over continental Europe.

7. Final Remarks

[70] We have predicted the effects of tectonics on baseline rates within Europe using a suite of thin sheet models intended to sample the sensitivity of the results to changes the Atlantic Ridge forces and to the presence of lateral variations in lithospheric strength. We have compared these results to GIA predictions and to observed baseline rates relative to three reference sites; VAAS, ONSA, and POTS. Our analysis suggests that geodetically inferred deformation of the broad region represents a complex interplay between deformation associated Africa-Eurasia convergence, GIA, and Atlantic Ridge spreading. Furthermore, each of these signals has a distinct geometric impact on the European region, and this has been highlighted by predictions associated with the three reference sites. Not surprisingly, Africa-Eurasia boundary forces have the strongest impact on baselines rates within the southern part of Europe. While GIA strongly dominates the deformation signal for the northern (Fennoscandian) baselines, nonnegligible contributions from this process are evident for baselines within central and southern Europe. Southerly directed baselines from POTS and ONSA clearly indicate that tectonics plays an increasingly important role toward the Alpine front and Mediterranean domain. We also note that lateral variations in lithospheric strength have a major impact in moderating deformation patterns associated with tectonic forcing. We considered two classes of such models; the first was characterized by a stiffening of the Baltic Shield, while

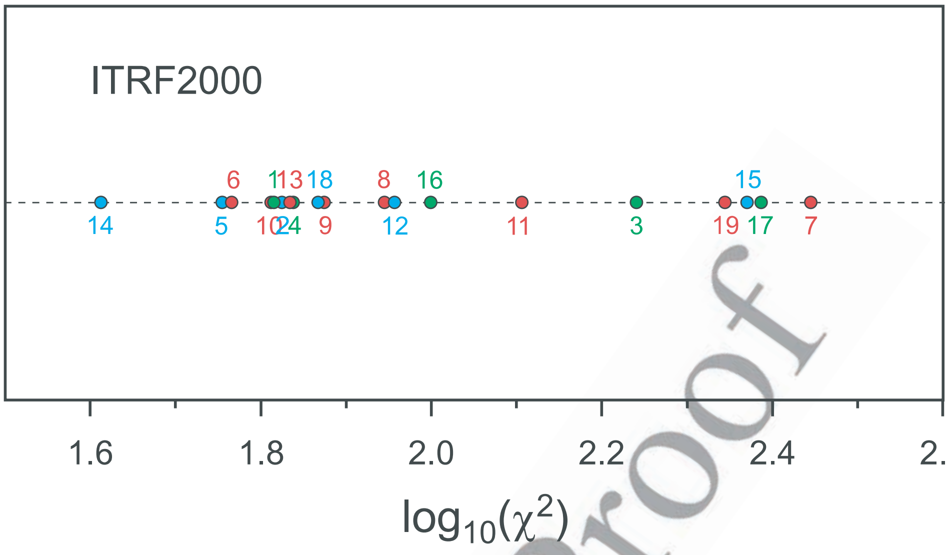

Figure 13. Results of the χ^2 analysis (see text for a detailed discussion) for the performance of the models listed in Table 1.

the second involved a weakening of the Mediterranean domain.

[71] When the ITRF2000 data set is considered, a combined model characterized by a tectonic prediction with a weakened lithosphere in the Mediterranean subdomain and the standard GIA prediction yields the best fit. This indicates that both intraplate tectonic deformations and GIA must be taken simultaneously into account to reconcile the broad style of intraplate deformation in Europe.

Appendix A: Mathematical Details of the Tectonic Model

[72] Introducing equation (10) into equations (7) and (8), we obtain

$$-\frac{\partial}{\partial\theta}p + \frac{\partial}{\partial\theta}\tau_{\theta\theta} + \frac{1}{\sin\theta}\frac{\partial}{\partial\phi}\tau_{\theta\phi} + r\frac{\partial}{\partial r}\tau_{\theta r} + (\tau_{\theta\theta} - \tau_{\phi\phi})\cot\theta + 3\tau_{\theta r} = 0 \tag{A1}$$

$$-\frac{1}{\sin\theta}\frac{\partial}{\partial\phi}p + \frac{\partial}{\partial\theta}\tau_{\phi\theta} + \frac{1}{\sin\theta}\frac{\partial}{\partial\phi}\tau_{\phi\phi} + r\frac{\partial}{\partial r}\tau_{\phi r} + 3\tau_{\phi r} + 2\tau_{\phi\theta}\cot\theta = 0 \tag{A2}$$

[73] Assuming zero basal shear stresses and the dominance of horizontal tectonic forces, the components $\sigma_{r\theta}$, $\sigma_{r\phi}$ within these general equations can be neglected. The corresponding equations, averaged through the lithospheric thickness, take the following form:

$$-\frac{\partial}{\partial\theta}\overline{p} + \frac{\partial}{\partial\theta}\overline{\tau}_{\theta\theta} + \frac{1}{\sin\theta}\frac{\partial}{\partial\phi}\overline{\tau}_{\theta\phi} + (\overline{\tau}_{\theta\theta} - \overline{\tau}_{\phi\phi})\cot\theta = 0 \tag{A3}$$

$$-\frac{1}{\sin\theta}\frac{\partial}{\partial\phi}\overline{p} + \frac{\partial}{\partial\theta}\overline{\tau}_{\phi\theta} + \frac{1}{\sin\theta}\frac{\partial}{\partial\phi}\overline{\tau}_{\phi\phi} + 2\overline{\tau}_{\phi\theta}\cot\theta = 0 \tag{A4}$$

where we must emphasize that all the fields are averaged values over the lithospheric thickness.

[74] In order to obtain the average pressure, $\overline{p}$, we follow, in spherical geometry, the procedure described by *England and McKenzie* [1981]. We use the third Navier-Stokes equation

$$\frac{1}{r}\frac{\partial}{\partial\theta}\sigma_{r\theta} + \frac{1}{r\sin\theta}\frac{\partial}{\partial\phi}\sigma_{r\phi} + \frac{\partial}{\partial r}\sigma_{rr} + \frac{1}{r}(2\sigma_{rr} - \sigma_{\theta\theta} - \sigma_{\phi\phi} + \sigma_{r\theta}\cot\theta) + f_r = 0 \tag{A5}$$

which becomes, after having neglected the shear stress components,

$$\frac{\partial}{\partial r}\sigma_{rr} + \frac{1}{r}[2\sigma_{rr} - \sigma_{\theta\theta} - \sigma_{\phi\phi}] + f_r = 0 \tag{A6}$$

Making use of the incompressibility condition and assuming that the radial strain rate is zero, we finally obtain

$$\frac{\partial}{\partial r}\sigma_{rr} + f_r = 0 \tag{A7}$$

with $f_r = -\rho\, g$, where g is the gravity and ρ is the density. Integrating equation (A7) over the lithospheric thickness, we get

$$\sigma_{rr} = g\int_{r_o}^{r}\rho dr + f(\theta,\phi) \tag{A8}$$

where r_o defines the base of the lithosphere. Since the system is assumed in isostatic equilibrium,

$$f(\theta,\phi) = -p_o \tag{A9}$$

(pressure at the base of the lithosphere). Thus, in terms of deviatoric stress, equation (A9) becomes

$$\tau_{rr} - p = g\int_{r_o}^{r}\rho dr - p_o \tag{A10}$$

or

$$p = p_o - g\int_{r_o}^{r} \rho dr + \tau_{rr} \tag{A11}$$

The average pressure required by equations (A3) and (A4) is obtained by integrating this expression over the total thickness of the thickened lithosphere:

$$\bar{p} = \frac{1}{L+h}\int_{r_o}^{r_o+L+h} p(r)dr \tag{A12}$$

where h is the topographic altitude. This integration yields

$$\bar{p} = \frac{1}{2}g\rho_m L + \frac{1}{2}g\rho_c\frac{S^2}{L}\left(1-\frac{\rho_c}{\rho_m}\right) \tag{A13}$$

where ρ_m, ρ_c, L, and S are the densities of the mantle and crust and the thickness of the lithosphere and crust, respectively.

[75] Using expressions (1), (2), and (4) for $\tau_{\theta\theta}$, $\tau_{\phi\phi}$ and $\tau_{\theta\phi}$ in equation (A3), and making use of expression (A13) for $\bar{\rho}$, we derive our final result:

$$\begin{aligned}&\frac{\partial}{\partial\theta}\left[2\bar{\mu}\left(\frac{\partial}{\partial\theta}u_\theta + u_r\right)\right] + \frac{1}{\sin\theta}\frac{\partial}{\partial\phi}\left[\bar{\mu}\left(\frac{1}{\sin\theta}\frac{\partial}{\partial\phi}u_\theta + \frac{\partial}{\partial\theta}u_\phi - u_\phi\cot\theta\right)\right]\\ &\quad + \left[2\bar{\mu}\left(\frac{\partial}{\partial\theta}u_\theta - \frac{1}{\sin\theta}\frac{\partial}{\partial\phi}u_\phi - u_\theta\cot\theta\right)\right]\\ &\quad \cot\theta = \frac{g\rho_c R}{2L}\left(1-\frac{\rho_c}{\rho_m}\right)\frac{\partial}{\partial\theta}S^2\end{aligned} \tag{A14}$$

$$\begin{aligned}&\frac{\partial}{\partial\theta}\left[\bar{\mu}\left(\frac{1}{\sin\theta}\frac{\partial}{\partial\phi}u_\theta + \frac{\partial}{\partial\theta}u_\phi - u_\phi\cot\theta\right)\right]\\ &\quad + \frac{1}{\sin\theta}\frac{\partial}{\partial\phi}\left[2\bar{\mu}\left(\frac{1}{\sin\theta}\frac{\partial}{\partial\phi}u_\phi + u_\theta\cot\theta + u_r\right)\right]\\ &\quad + \left[2\bar{\mu}\left(\frac{\partial}{\partial\theta}u_\phi + \frac{1}{\sin\theta}\frac{\partial}{\partial\phi}u_\theta - u_\phi\cot\theta\right)\right]\cot\theta\\ &= \frac{g\rho_c R}{2L}\left(1-\frac{\rho_c}{\rho_m}\right)\frac{1}{\sin\theta}\frac{\partial}{\partial\phi}S^2\end{aligned} \tag{A15}$$

where R is the radius of the spherical Earth.

[76] **Acknowledgments.** This research was funded by the Italian Ministry of Universities and Research (MIUR) under the project entitled "A multidisciplinary monitoring and multiscale study of the active deformation in the northern sector of the Adria plate" (COFIN 2002). All figures were created using GMT plotting software [*Wessel and Smith*, 2001]. The authors thank Riccardo Barzaghi, Bruno Crippa, and Fernando Sanso for fruitful suggestions. The authors also thank the Associate Editor and two anonymous reviewers for their constructive remarks.

References

Altamimi, Z., P. Sillard, and C. Boucher (2002), ITRF2000: A new release of the International Terrestrial Reference Frame for earth science applications, *J. Geophys. Res.*, *107*(B10), 2214, doi:10.1029/2001JB000561.

Bassin, C., G. Laske, and G. Masters (2000), The current limits of resolution for surface wave tomography in North America, *Eos Trans. AGU*, *81*(48), Fall Meet. Suppl., Abstract S12A-03.

Dziewonski, A. M., and D. L. Anderson (1981), Preliminary Reference Earth Model (PREM), *Phys. Earth Planet. Inter.*, *25*, 297–356.

England, P., and D. McKenzie (1983), Correction to: A thin viscous sheet model for continental deformation, *Geophys. J. R. Astron. Soc.*, *73*, 523–532.

Grunthal, G., and D. Stromeyer (1992), The recent crustal stress field in central Europe: Trajectories and finite element modeling, *J. Geophys. Res.*, *97*, 11,805–11,820.

James, T. S., and A. Lambert (1993), A comparison of VLBI data with the ICE-3G glacial rebound model, *Geophys. Res. Lett.*, *20*, 871–874.

Jiménez-Munt, I., R. Sabadini, A. Gardi, and G. Bianco (2003), Active deformation in the Mediterranean from Gibraltar to Anatolia inferred from numerical modeling and geodetic and seismological data, *J. Geophys. Res.*, *108*(B1), 2006, doi:10.1029/2001JB001544.

Johansson, J. M., et al. (2002), Continuous GPS measurements of postglacial adjustment in Fennoscandia 1. Geodetic results, *J. Geophys. Res.*, *107*(B8), 2157, doi:10.1029/2001JB000400.

Lambeck, K., C. Smither, and P. Johnston (1998), Sea-level change, glacial rebound and mantle viscosity for northern Europe, *Geophys. J. Int.*, *134*, 102–144.

Marotta, A. M., and R. Sabadini (2002), Tectonic versus glacial deformation in Europe, *Geophys. Res.*, *29*, 73-1/73-4.

Marotta, A. M., U. Bayer, M. Scheck, and H. Thybo (2001), The stress field below the NE German Basin: Effects induced by the Alpine collision, *Geophys. J. Int.*, *144*, F8–F12.

McClusky, S., et al. (2000), Global Positioning System constraints on plate kinematics and dynamics in the eastern Mediterranean and Caucasus, *J. Geophys. Res.*, *105*, 5695–5719.

Milne, G. A., J. X. Mitrovica, and J. L. Davis (1999), Near-field hydro-isostasy: The implementation of a revised sea-level equation, *Geophys. J. Int.*, *139*, 464–482.

Milne, G. A., J. L. Davis, J. Mitrovica, H. G. Scherneck, J. M. Johansson, M. Vermeer, and H. Kouvula (2001), Space geodetic constrains on glacial isostatic adjustment in Fennoscandia, *Science*, *291*, 2385–2391.

Mitrovica, J. X., J. L. Davis, and I. I. Shapiro (1993), Constraining proposed combinations of ice history and Earth rheology using VLBI determined baseline rates in North America, *Geophys. Res. Lett.*, *20*, 2387–2390.

Mitrovica, J. X., J. L. Davis, and I. I. Shapiro (1994a), A spectral formalism for computing three-dimensional deformations due to surface loads: 1. Theory, *J. Geophys. Res.*, *99*, 7057–7073.

Mitrovica, J. X., J. L. Davis, and I. I. Shapiro (1994b), A spectral formalism for computing three-dimensional deformations due to surface loads, 2. Present-day glacial isostatic adjustment, *J. Geophys. Res.*, *99*, 7075–7101.

Mitrovica, J. X., G. A. Milne, and J. L. Davis (2001), Glacial isostatic adjustment on a rotating Earth, *Geophys. J. Int.*, *147*, 562–579.

Molnar, P., T. J. Fitch, and F. T. Wu (1973), Fault plane solutions of shallow earthquakes and contemporary tectonics in Asia, *Earth Planet. Sci. Lett.*, *19*, 101–112.

Peltier, W. R. (1974), The impulse response of a Maxwell Earth, *Rev. Geophys.*, *12*, 649–669.

Peltier, W. R. (1995), VLBI baseline variations from the ICE-4G model of postglacial rebound, *Geophys. Res. Lett.*, *22*, 465–468.

Peltier, W. R. (1998), Postglacial variations in the level of the sea: Implications for climate dynamics and solid-Earth geophysics, *Rev. Geophys.*, *36*, 603–689.

Richardson, R. M., and L. Reding (1991), North American plate dynamics, *J. Geophys. Res.*, *96*, 12,201–12,223.

Richardson, R. M., S. C. Solomon, and N. H. Sleep (1979), Tectonic stress in the plates, *Rev. Geophys.*, *17*, 981–1019.

Schubert, G., D. L. Turcotte, and P. Olson (2001), *Mantle Convection in the Earth and Planets*, 940 pp., Cambridge Univ. Press, New York.

Turcotte, D. L., and G. Schubert (2002), *Geodynamics*, 237 pp., Cambridge Univ. Press, New York.

Tushingham, A. M., and W. R. Peltier (1991), ICE-3G: A new global model of late Pleistocene deglaciation based upon geophysical predictions of postglacial relative sea level change, *J. Geophys. Res.*, *96*, 4497–4523.

Wessel, P., and W. M. F. Smith (2001), New improved version of Generic Mapping Tools released, *Eos Trans. AGU*, *79*, 579.

A. M. Marotta and R. Sabadini, Geophysics Section, Department of Earth Sciences, University of Milan, L. Cicognara 7, I-20129, Milan, Italy. (anna.maria.marotta@unimi.it; roberto.sabadini@unimi.it)

J. X. Mitrovica, Department of Physics, University of Toronto, 60 St. George Street, Toronto, Ontario, Canada M5S 1A7. (jxm@terra.physics.utoronto.ca)

G. Milne, Department of Geological Sciences, University of Durham, South Road, Durham, DH1 3LE, UK. (g.a.milne@durham.ac.uk)